1-1-2011

Modeling and Verification of a Multi-section Continuum Robot

Krishna Turlapati

MODELING AND VERIFICATION OF A MULTI-SECTION CONTINUUM ROBOT

By

Krishna Turlapati

A Thesis
Submitted to the Faculty of
Mississippi State University
in Partial Fulfillment of the Requirements
for the Degree of Masters of Science
in Computer Engineering
in the Department of Electrical and Computer Engineering

Mississippi State, Mississippi

April 2011

MODELING AND VERIFICATION OF A MULTI-SECTION CONTINUUM ROBOT

By

Krishna Turlapati

Approved:

Bryan A. Jones Assistant Professor of Electrical and Computer Engineering (Major Advisor and Director of Thesis)	Robert B. Reese Associate Professor of Electrical and Computer Engineering (Committee Member)
Sherif Abdelwahed Assistant Professor of Electrical and Computer Engineering (Committee Member)	James E. Fowler Professor of Electrical and Computer Engineering (Graduate Program Director)
Sarah A Rajala Dean of Bagley College of Engineering	

Name: Krishna Turlapati

Date of Degree: April 30, 2011

Institution: Mississippi State University

Major Field: Computer Engineering

Major Professor: Dr. Bryan A Jones

Title of Study: MODELING AND VERIFICATION OF A MULTI-SECTION CONTINUUM ROBOT

Pages in Study: 70

Candidate for Degree of Masters of Science

Continuum robots mimic the principle of a special biological structure known as the muscular hydrostat. These robots have an ability to bend at any location on along its backbone and have potential applications in disaster relief, medical surgeries and nuclear waste disposal. This thesis presents the modeling and verification of a multi-section continuum robot by applying the Cosserat theory of rods. Next, 2D verification is performed on a continuum robot based on a backbone composed of a nickel titanium alloy. In addition, the thesis develops the theoretical foundations for a cable-driven continuum robot by studying the effects of cable guide mass which cause additional deformation of the robot The results of this thesis show that the multi-section model is accurate within 3.4% in predicting the Cartesian tip coordinates, and the model with the cable guides accurate within 1.26% error in predicted versus the observed Cartesian tip coordinates of the backbone.

Key words: Biologically inspired robots, Continuum robots, Continuum, Verification, Model, Statics, Muscular Hydrostat.

DEDICATION

To God, for giving me strength and confidence through the many obstacles in my path; who, I believe was helping, me in the form of my parents Dr. Turlapati Lakshmi Narasimha Prasad & Turlapati Sarada and my advisor/mentor Dr. Bryan A Jones.

ACKNOWLEDGEMENTS

My sincere thanks to Dr. Santosh Seran, Dr. Sunderajan Srinivasan and, Jeremy Yarber for their unconditional support and cooperation. To my friends Roberto and Ricky for inspiring and helping me in my endeavors.

To Professor Chivukula Ramakrishna Sarma, for introducing me to microcontrollers. To my loving sisters Keerthi akka, Sowmya (Cute akka), Anne, to my friends Naveen, Bhavya, Karthik, Srinivas, Shashank, Bharath without my association with them I would not be where I am.

Finally, I would like to thank the Department of Electrical and Computer Engineering, Robotics Research Laboratory and Mississippi State University for support and cooperation. Go Dawgs!!

TABLE OF CONTENTS

Page

LIST OF TABLES

LIST OF FIGURES

FIGURE Page

CHAPTER I

INTRODUCTION

Continuum robots mimic the principle of a special biological structure known as muscular hydrostat. An elephant trunk, mammalian tongues, and octopus arms provide examples of the biological species which extensively use this hydrostatic muscular structure [1]. The invertebrate mechanism of the octopus arms provides agility in catching prey and locomotion. Similarly, the elephant trunk can bend with ease, exhibits strength while carrying logs of wood. Researchers are being inspired by amazing capabilities exhibited by the biological structures and are mimicking the fundamental properties using robotic counterparts.

Like their biological counterparts, continuum robots do not posses any rigid links or discrete joints; instead, these robots are modeled on a flexible backbone which allows unconstrained movement at any point on its structure. This unique flexibility enables a wide range of practical applications which prove difficult to achieve with traditional rigid-link robots. Potential applications of continuum robots include search and rescue [2], exploring unstructured environments [3], handling hazardous nuclear material [4], performing complex medical examinations and surgeries [5-16], in addition to many other applications discussed in [17].

Several barriers prevent the widespread use of continuum robots in these essential tasks. Primarily the ability to reach a particular location in the workspace of a continuum robot is defined as accessibility can be improved with multi-sections. Next, for a cable

actuated robot the cable guides produce additional deformations on the backbone. There is a need to account these additional deformations for a cable driven robot. Alternate torque calculations using cable length can help in shaping the robot without requiring usage of load cells. The following chapters present solutions to these important problems.

In particular, the second chapter presents an overview of the approach used to determine the 3-D shape of a single section continuum robot [18] by applying Cosserat theory of rod presented by Antman [19]. This theory treats any rod with few mathematical approximations and geometric assumptions. This model allows the rod to experience bending and shear strains at every point. With a set of initial and boundary conditions, this chapter concludes by formulating the necessary differential equations which describe the mechanics of deformations produced in the rod. This powerful model, however, applies only to a single-section robot.

Therefore, chapter three discusses extension to the model in order to define the statics of a multi-section model. A single-section design can be extended to multi-sections via analysis of the section transitions. A continuous backbone without any section transitions can be treated as a single section. The analysis of a multi-section continuum robot begins by treating the section transition as a discontinuity. It is essential to determine the jump conditions which define this discontinuity and therefore connect one section to the next section. These jump conditions are derived by applying the principles of mechanics and kinematics at the section transition. This results in a set of new initial conditions necessary in computing the shape of the remaining sections.

This chapter also discusses the effects of cable guide mass on the robot. The main components of a cable-driven mechanism are the cable guides and cables. The cable guides provide a means for the cables to run the length of the robot. The inclusion of the

cable guides causes additional deformation to rod; two methods are presented to account this additional mass. First, the average mass model takes the mass of rod and cable guides together. Alternately, since cable guides are spaced out evenly, the second approach, termed the accurate mass method, reflects the change in the density and the cross sectional area due to the presence and absence of the cable guide through the length of the rod.

Finally, the chapter concludes by nothing that cable lengths act as valuable source for determining the shape of the robot. A set of three cables separated by 120 degrees are passed through the cable guides. The length of each cable for a given tip loading is derived for a single section continuum manipulator with circular cable guides, opening the door for the use of simple, economic cable length sensors such as encoders to determine the shape of a continuum robot.

Chapter four presents the verification of the multi-section static model and of the effects of cable guide mass. The test bench comprises of a laser-etched grid, balances, rod clamps, and weights. To validate the multi-section model, a nickel-titanium (NiTi) shape memory alloy is used as the backbone of the continuum robot. The rod clamps provide a way to mount the NiTi on the laser-etched grid. A set of weights provides a wide range of tip loading. The rod is mounted on the laser etched grid using the rod clamps and, since it is a multi-section robot comprised of two sections, two sets of weights are attached at the end of each of the two sections. The predicted and actual Cartesian tip locations of both the sections are measured. Next, a set of five circular cable guides laser cut from acrylic are press fit on the rod. A single cable is passed through these five guides, then the change in length of the cable for set of tip loadings are recorded. Comparison of these experimental results helps to assess the accuracy of the various models developed.

Specifically, the results of this thesis show that the developed multi-section model is accurate to within 3.4% in predicting the Cartesian tip coordinates and the model with the cable guides shows less than 1.26% error in predicted versus the observed Cartesian tip coordinates of the trunk with the cable guides. The following chapter begins this process by presenting a single-section model for a continuum robot.

CHAPTER II

THREE-DIMENSIONAL STATICS OF A CONTINUUM ROBOT

2.1 Introduction

Continuum robots are biologically inspired, hyper-redundant manipulators built on a flexible backbone. The flexible backbone mimics the behavior of an octopus arm, an elephant's trunk, squid tentacles and mammalian tongues. These biological structures do not have any rigid skeletal system but instead have a group of muscles which operate on a constant volume principle. Due to this principle, changes to the cross-sectional area and its shape provide the organism the ability to extend, bend, and twist by producing an inverse change in the length of the organ. Organisms operating on this principle are termed as muscular hydrostats [1]. With the help of this muscular arrangement, an elephant trunk is capable of curling over a log of wood, octopus arms can bend and extend while catching prey and locomoting, and mammalian tongues can twist and bend while consuming food. In a similar way, the flexible backbone of a continuum robot mimics the behavior of the muscular hydrostats. Hence, the flexible backbone of a continuum robot can be used to curl around objects for grasping or can be used like an octopus arm for exploring unstructured environments and have many potential applications because of their ability to bend along any point on the backbone.

With these unique capabilities, continuum robots are natural candidates for use in search-and-rescue operations [2], in performing medical surgeries such as the use of an active cannula [14, 17, 20], and when performing medical examinations such as

endoscopy [10-12] and colonoscopy [6-9]. They also find application in hot cell decontamination [21], open loop grasping [22] and many more areas as detailed in [17].

The accessibility and accuracy of the tip of a continuum arm plays a vital role in many applications. Accessibility, the ability of a continuum trunk to reach a particular location in its workspace, poses a challenge in unstructured and confined environments. One definition for accuracy is the difference between predicted Cartesian end effector locations of a continuum trunk obtained from the model with the observed experimental values on a physical robot. For instance, in search-and-rescue operations, a continuum robot is required to bend in order to pass through debris. Also, in medical surgeries due to lack of space, accessing a particular target organ would require additional degrees of freedom. Enhanced accessibility leads to lower accuracy due to the increased complexities in the physical structure. However, by careful design and improved modeling, accessibility and accuracy can be improved.

The primary means of enhancing the accessibility in continuum robots is by using a multiple section continuum trunk. A set of serially connected, single section trunks form a multiple section arrangement capable of bending in complex shapes, providing enhanced accessibility.

The most common models [17] which predict the tip location of a continuum robot lack accuracy, due to a simplifying assumption which excludes the effectors gravity on the robot's shape. Hence, an improved model incorporating the underlying physical properties of the backbone and the deformations due to gravity loading would significantly enhance the accuracy of the continuum manipulator.

This thesis presents a 3-D statics model of a cable driven multi-section continuum robot which improves both its accuracy and accessibility. The accuracy is enhanced by

using an approach which models the underlying bending and deformations of a continuum trunk in presence of gravity [23]. The accessibility is provided by using a multi-section arrangement, in contrast to the cable driven, single section robots designed at our robotics research laboratory [18, 24]. This thesis also provides a generic platform for testing and verification of these models.

2.2 Background

There are multiple approaches to model a continuum robot. Two widely used approaches are the constant curvature approximation and the application of Cosserat rod theory. The constant curvature model approximates the curved shape of the robot as an arc of a circle [17]. In the absence of external loading such as gravity, moments applied at the tip of the trunk cause the backbone of the continuum robot to bend in a constant arc. This assumption allows in the development of an analytical formulation for traditional forward and inverse kinematics. This model has been successfully implemented in robots which could perform medical surgeries, such as an active cannula [14, 17, 20] and in medical examinations such as colonoscopes [6-9], endoscopes [10-12], in designing various robots such as OctArm [22, 25, 26], Air-Octor [27], [24], and in many other applications [17]. Some robots built using the constant curvature modeling assumption demonstrated high accuracy [28] because the stiffness of the backbone counteracts the effects of the gravity. However, in the common and more general case, the presence of gravity creates a significant difference between the shape of the predicted versus the actual robot [22, 24, 29, 30]. For example, the constant curvature model produces an average error of 50% in predicted verses actual position for the OctArm robot [30]. These problems demonstrate the need for a more accurate model.

Cosserat rod theory provides an alternative way to model continuum robots. Work by Antman [23] presents the deformation of a thin elastic rod with few geometrical and mathematical assumptions. This approach has been extended to continuum robots by modeling the continuous backbone as a thin elastic rod in 3-D space. This model, in contrast to the constant curvature model, incorporates the presence of forces and torques acting on the backbone in 3-D while the constant curvature model includes only single moment at the tip of the backbone. Also, the model accounts for internal deformations produced by shear and bending strain along every point on the rod

This more accurate approach based on Cosserat rod theory provides a significant increase in accuracy in predicting the tip location of the continuum trunk. A 3-D model built using Cosserat rod theory, experimentally validated on OctArm, shows less than five percent average error in predicting the tip location measured in centimeters [30], compared to 50% error with the constant curvature model. Recently, 2-D verification on a 3-D static model built using the Cosserat rod framework, based on experimental measurements of a nickel titanium rod, shows an average error of 0.61% in the predicted versus the measured Cartesian tip coordinates of the physical rod [18]. A geometrically exact model developed based on Cosserat rod theory, for active cannulas using Nickel Titanium alloy tubes [31] achieved a 2.91 mm error in their predictions of the tip locations. Although the existing models based on the comprehensive approach demonstrated significant accuracy and accessibility, they have been restricted to medical applications or the model was developed to suit OctArm.

However, a generic 3-D static multi-section continuum model based on Cosserat rod theory and the usage of cables for actuation has not been studied and implemented yet. The 3-D statics presented in [18] describe the shape of a single section continuum

robot. This model can be extended to multiple sections by linking individual single-section structures. The main advantage of this model [18] is that there is no need for additional links, joints or shocks to realize a multi-section structure. This chapter focuses on reviewing the 3-D statics presented in [18]. The next chapter provides the extensions for a multi-section model.

2.3 Overview of 3D Statics

The continuous backbone of a continuum robot is treated as a curve and is parameterized with an unstretched length, referred by the variable s as shown in 1. To specify the global coordinates of a particular point c along the rod, a three element vector $\mathbf{r}(c) \in \mathbb{R}^3$ is used. A rotation matrix $\mathbf{R}(c) \in SO(3)$ gives the orientation of the rod at this point with respect to the global frame by defining a local coordinate frame formed using elements of the rotation matrix.

The shape of the rod is determined by the spatial linear velocity vector $\mathbf{v}^l(s)$ and spatial angular velocity vector $\mathbf{u}^l(s)$ as shown in 2 and 3, which are defined at every point s on the rod. The superscript l denotes that the element resides in the local coordinate frame. For any vector $\mathbf{a}^l$, in local coordinates can be transformed to

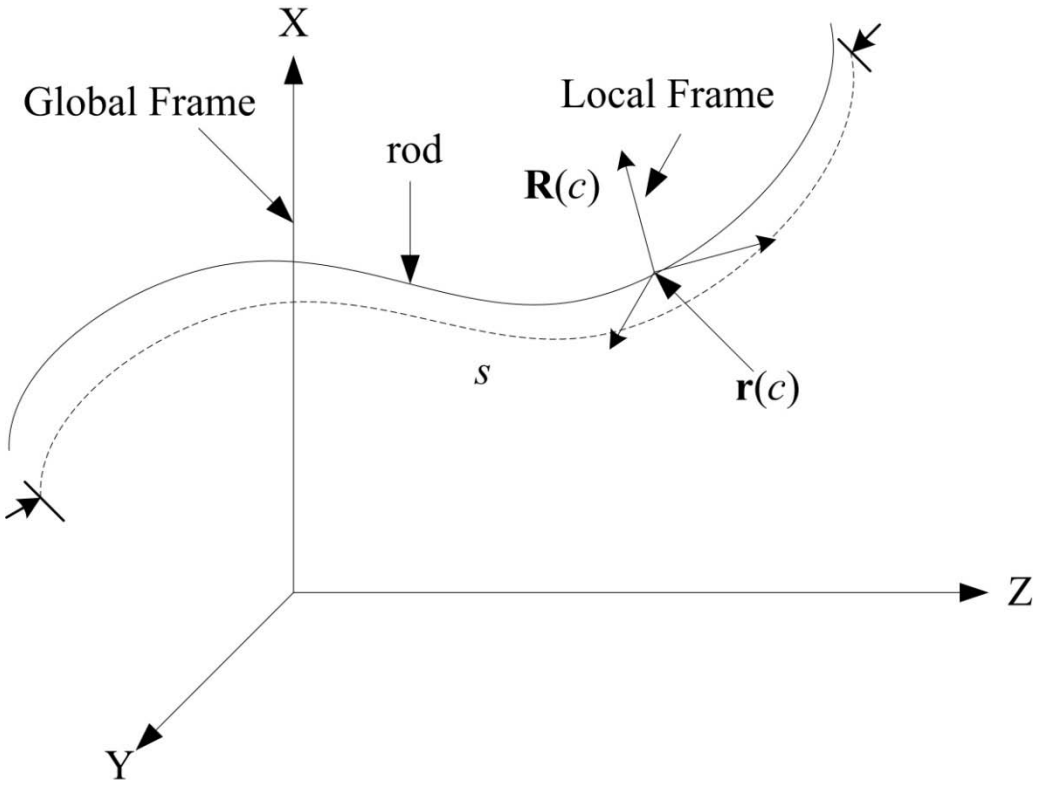

Figure 2.1 The continuous backbone is represented by a curve with the reference length s denoted by a dotted line. At an arbiatrary point c along the rod, $\mathbf{r}(c)$ gives the position in global coordiantes and $\mathbf{R}(c)$, the rotation matrix, describes the orientation of the rod in global cooridinates.

the global coordinate frame by multiplying with the rotation matrix $\mathbf{a} = \mathbf{R}\mathbf{a}^l$; to map it back to a local coordinate, an element in the global coordinate frame is multiplied by $\mathbf{R}^{\mathrm{T}}$.

The spatial velocity vector $\mathbf{v}^l(s)$ defines the shear in the rod illustrated in Figure 2.2. This vector is composed of three elements given by

$$\mathbf{v}^l(s) = \begin{bmatrix} v_1^l & v_2^l & v_3^l \end{bmatrix}^{\mathrm{T}} \tag{2.1}$$

where $v_{1,2}^l$ are shear strains and v_3^l gives the dilation or stretch. The stretch v_3^l is parameterized by its unstretched length; that is, $v_3^l = 1$ implies no shear or stretch, while $0 < v_3^l < 1$ implies compression and $v_3^l > 1$ is extension or stretch.

The rod extends along the *z* axis, Figure 2(a) shows the shear strain produced by v_1^l along in the *xz* plane while Figure 2(b) shows the stretch v_3^l along the *z* axis; the initial position is denoted by s_o and final position by s_f. The internal shears which are spatial velocities produces a sliding motion along the direction of shear. This velocity is also represented by the internal position vector $\dot{\mathbf{r}}(s)$. The dot denotes that it is a derivative with respect to the reference length s. The local coordinate frame given by the rotation matrix $\mathbf{R}(s)$ slides along the *xz* plane without changing the orientation due to the effects of shear strain, illustrated in Figure 2(a). The direction of propagation is along the vector $\dot{\mathbf{r}}(s)$ and β is the angle between the direction of propagation and the local coordinate frame also known as shear angle.

The spatial angular velocity vector $\mathbf{u}^l(s)$ defines the bending strain produced in the rod. This vector is composed of three elements given by

$$\mathbf{u}^l(s) = \begin{bmatrix} u_1^l & u_2^l & u_3^l \end{bmatrix}^{\mathrm{T}} \tag{2.2}$$

where $u_{1,2}^l$ specify bending about the *x* and *y* axes and u_3^l is the twist or torsion produced about the *z* axis. Figure 2.3 illustrates the bending and twist experienced by the rod. The orientation of the local coordinate frame changes due to the bending strains $\mathbf{u}^l$ as shown in Figure 2.3(a) and Figure 2.3(b). Specifically, in Figure 2.3(b) a reference line AA' is chosen before the twist is applied. On application of the twist u_3^l the reference line AA' shows torisional deformation.

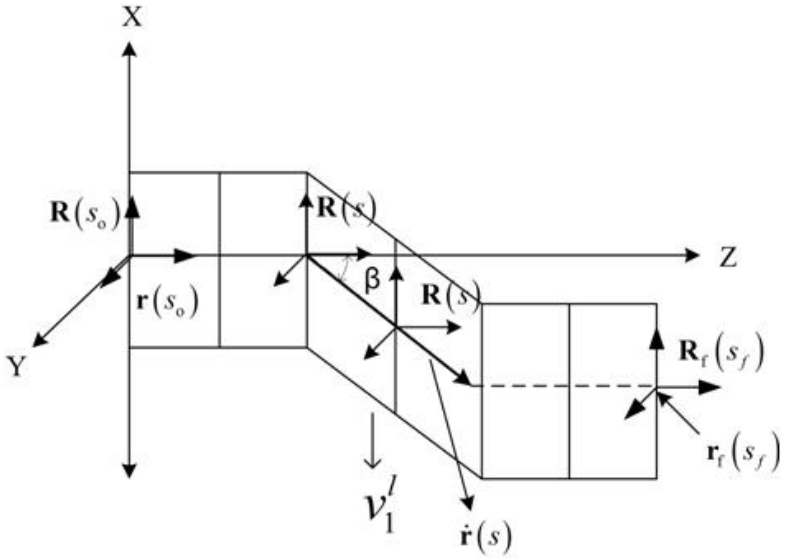

(a)

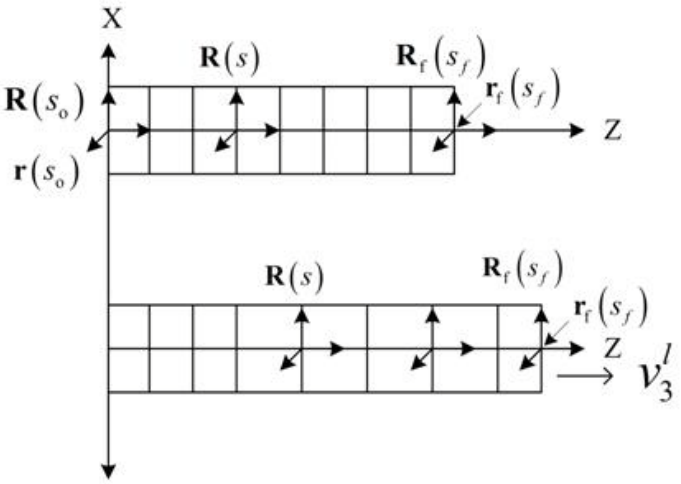

(b)

Figure 2.2 Side view of a thin rod placed along the *z* axis. In (a), the shear velocity v_1^l produces a shear along the *x* axis; initial and final position and orientation vectors are also shown. Note that identical initial and final coordinate frames shows that no bending occurred. Instead, the local coordinate frame slides along the direction of shear. In (b), the stretch v_3^l causes the rod to extend along the *z* axis.

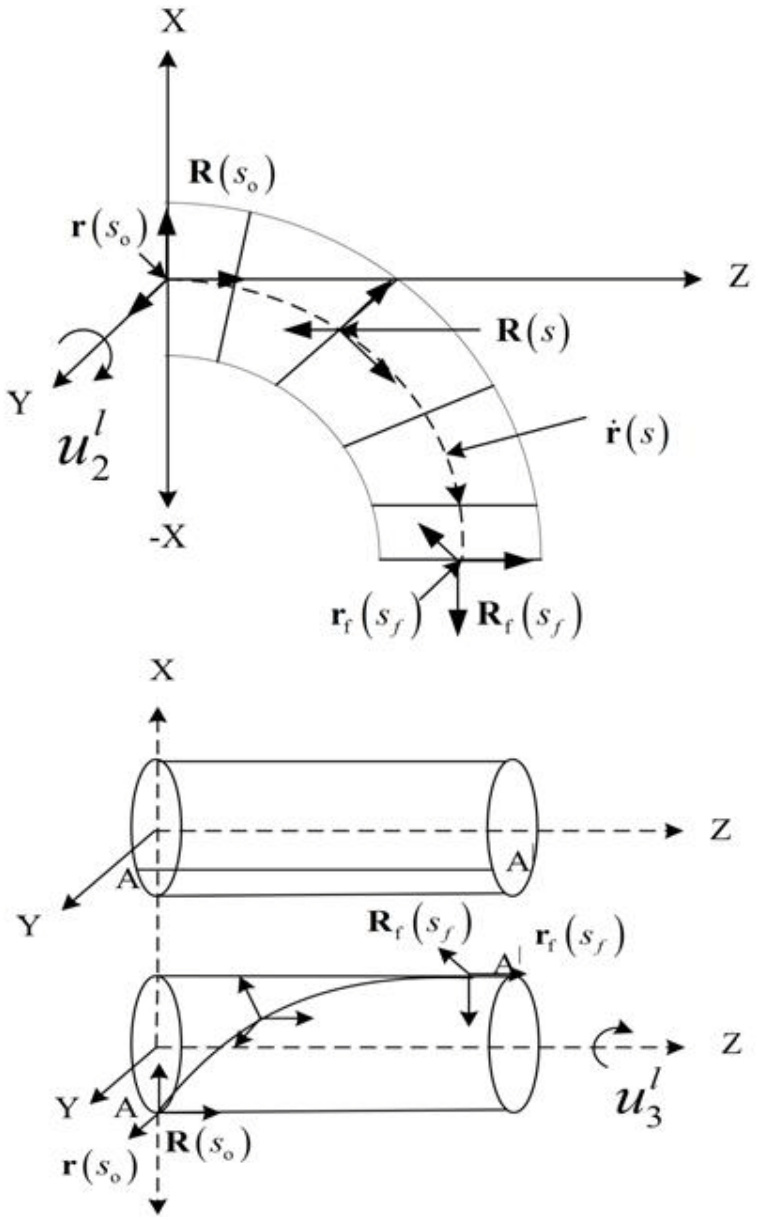

Figure 2.3 Side view of a thin rod placed along the *z* axis. In (a), the bending strain u_2^l produces a bending along the *y* axis; comparison of the initial and final position and orientation vectors shows the results of this deformation as the local coordinate frame changes orientation due to bending. In b): The twist strain u_3^l causes the rod to twist about the *z* axis. The reference line AA' shows a torisional deformation

2.4 3D Static Analysis

The previous section provides an overview of the elements which define the deformation of one infinitesimal slice of the rod. To see the global effects of these deformations, the analysis is done in three steps. The first step provides the initial and boundary conditions and the arrangement of the rod in global coordinates. In the second section, kinematics describes the shape and orientation of a particular point on the rod using the shear and bending strains. The last section, Mechanics, connects the internal and external forces and torques acting on the rod with their corresponding displacements obtained from kinematics. This section also provides constitutive equations which relate the internal forces and torques to the shear and bend strains. Finally, by combining all the three sections, a set of differential equations which describe the shape of the rod in 3-D are obtained.

2.5 Initial and Boundary Conditions

This model is subject to the following initial conditions: the rod is placed at the origin of global coordinate system, implying $\mathbf{r}(0) = [0 \quad 0 \quad 0]^{\mathrm{T}}$, and extends along the z axis. The rotation matrix $\mathbf{R}(0)$ provides the initial orientation of the rod. If there is no initial rotation, then $\mathbf{R}(0)$ is treated as an identity matrix, $\mathbf{R}(0) = \mathbf{I}$. To counteract external torque $\boldsymbol{\tau}_{tip}$ applied to the tip of the rod, there exists an unknown initial bending $\mathbf{u}^l(0)$. This initial bending $\mathbf{u}^l(0)$ is found iteratively by minimizing the error between the actual tip torque $\boldsymbol{\tau}_{tip}$ and calculated tip torque. Hence, finding the initial bending $\mathbf{u}^l(0)$ requires a solution of the boundary condition $\boldsymbol{\tau}_{tip}$. The shear strains $\mathbf{v}^l$ are computed analytically. The initial and boundary conditions are summarized in Table 1.

Table 2.1 Shows the initial and boundary conditions

Initial Conditions		Boundary Conditions	
$\mathbf{r}(0)$	(*x, y, z*) of rod origin		
$\mathbf{R}(0)$	Initial orientation		
$\mathbf{u}^l(0)$	Initial bending (found iteratively)	$\boldsymbol{\tau}_{tip}$	Tip force (*known*)
$\mathbf{v}^l(0)$	Initial stretch and shear	$\boldsymbol{\nu}_{tip}$	Tip moment (*known*)

2.6 Kinematics

The change in position of a particular location on the rod in global coordinates is given by

$$\dot{\mathbf{r}}(s) = \mathbf{R}(s)\mathbf{v}^l(s). \tag{2.3}$$

where the dot indicates a derivative according to s, and $\mathbf{v}^l(s)$ is composed of the shear strains.

The orientation of a particular point in global coordinates is given by

$$\dot{\mathbf{R}}(s) = \mathbf{R}(s)\hat{\mathbf{u}}^l(s), \tag{2.4}$$

where $\mathbf{R}(s)$ is a rotation matrix and $\hat{\mathbf{u}}^l$ is a skew symmetric matrix defined by the 3×3 matrix

$$\hat{\mathbf{u}}^l = \begin{bmatrix} 0 & -u_3 & u_2 \\ u_3 & 0 & -u_1 \\ -u_2 & u_1 & 0 \end{bmatrix} \tag{2.5}$$

2.7 Mechanics

The mechanics section describes the shape of the rod by enforcing force and torque balances. The deformations produced by the resultant forces and torques are connected to kinematics using constitutive equations. This section is divided in two components: the force balance and torque balance. The force balance equation sums all

the forces acting on the rod while the torque balance equation sums all the torques on the rod.

2.7.1 Force balance equation

Two classes of forces act on the rod. Contact force results from elastic deformations and causes one section of the rod to apply a restoring elastic force to another section of the rod. All other forces are termed body forces. The free body diagram shown in Figure 4 depicts these forces.

The contact force is defined by a three element vector $\mathbf{n}(s) \in \mathbb{R}^3$. The positive and the negative assignments for these forces are mere sign conventions. Consider a deformed segment from c to s on a rod as shown in Figure 2.4. The portion of the rod from $[s_1 \quad c]$experiences a negative force from the remaining section of the rod $(c \quad s_2]$ whereas the portion of the rod from$[s \quad s_2]$ exerts a positive force on the $[s_1 \quad s)$ portion of the rod. All the other forces acting on the rod between $[c \quad s]$other than the contact forces are termed body force or distributed loads; they are denoted by $\mathbf{f}(\xi)$, a force per reference unit length of the rod. All body forces acting on the rod between $[c \quad s]$is given by $\int_c^s \mathbf{f}(\xi) d\xi$

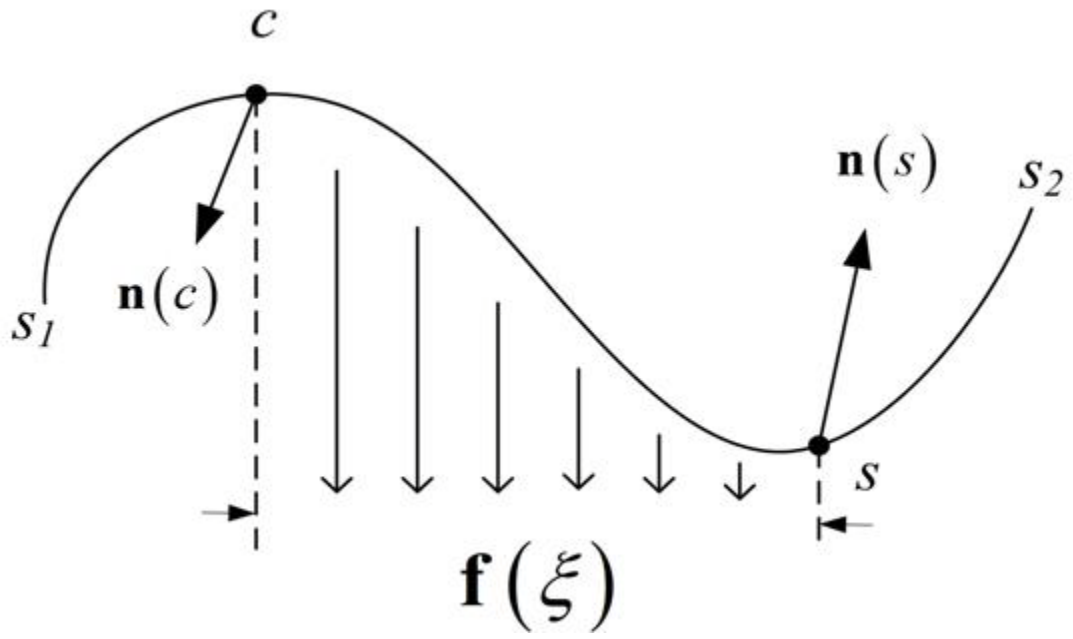

Figure 2.4 An illustration of force balance equation. The contact forces $\mathbf{n}(c)$ and $\mathbf{n}(s)$ are observed at points c and s on the rod, while $\mathbf{f}(\xi)$ denotes body forces, which comprise all forces acting on the rod between $[c \quad s]$.

The body force is expressed as force per unit reference length. By summing all the forces acting on the rod from $[c \quad s]$ at equilibrium,

$$\mathbf{n}(s)-\mathbf{n}(c)+\int_{c}^{s}\mathbf{f}(\xi)\,d\xi=\mathbf{0}. \tag{2.6}$$

Differentiating the above equation with respect to s, $\dot{\mathbf{n}}(s)+\mathbf{f}(s)=\mathbf{0}$. In the presence of gravity, at any arbitrary point along the backbone, the body force in the above equation can be represented by the mass per reference length times the acceleration due to gravity. The mass per reference length is expressed as ρA where ρ is the density of the rod at that point and A is the cross sectional area at that point. For a fixed density and area of cross section, the body force is given as,

$$\mathbf{f}(s)=\rho Ags\mathbf{e}_{g}, \tag{2.7}$$

where g is the acceleration due to gravity and $\mathbf{e}_g$ is the unit vector in the direction of gravity.

If a known force $\mathbf{v}_{tip}$ is present at the tip of the trunk then the force balance equation can be rewritten by changing s to s_{tip} and rewriting,

$$\mathbf{n}(c) = \mathbf{n}(s_{tip}) + \int_c^{s_{tip}} \mathbf{f}(\xi)\, d\xi = \mathbf{0}.$$

Specifically, $\mathbf{n}(s_{tip})$ can be replaced by $\mathbf{v}_{tip}$; by substituting, the above equation can be rewritten

$$\mathbf{n}(c) = \mathbf{v}_{tip} + \rho A g (s_{tip} - c)\mathbf{e}_g. \tag{2.8}$$

2.7.2 Constitutive equation

Constitutive equations describe the relation between the shear strains and the internal contact forces at any particular point along the rod. Contact forces are assumed to obey a linear Hookean relationship. The constitutive equation for the resultant contact force at an arbitrary point s in global coordinates is given by

$$\mathbf{n}(s) = \mathbf{R}\mathbf{D}\left(\mathbf{v}^l(s) - \mathbf{e}_e\right), \tag{2.9}$$

where $\mathbf{R}$ is the rotation matrix which maps the local internal force $\mathbf{n}^l(s)$ to the global frame, $\mathbf{D} = diag\left(\begin{bmatrix} D_1 & D_2 & D_3 \end{bmatrix}\right)$ are material constants analogous to the constant K in the linear Hookean relation $F = Kx$. In particular, $D_1 = D_2 = GA$, and $D_3 = EA$ where A is the area of the cross section, E is the modulus of elasticity of the material and G the shear modulus.

By substituting the constitutive equation in, $\mathbf{R}\mathbf{D}\left(\mathbf{v}^l(s) - \mathbf{e}_e\right) = \mathbf{v} + \rho A g (s_{tip} - c)\mathbf{e}_g$. Solving for $\mathbf{v}^l(s)$, the above equation can be reduced to

$$\mathbf{v}^l(s) = \mathbf{D}^{-1}\mathbf{R}^{\mathrm{T}}\left[\mathbf{v} + \rho A g (s_{tip} - s)\mathbf{e}_g\right] + \mathbf{e}_e \tag{2.10}$$

The shear strains at any point along the rod can be analytically computed with the above equation.

2.7.3 Moment balance

Three types of torques act on the rod. First, contact moments result from elastic deformations and cause one section of the rod to apply a restoring internal moment to another section of the rod. Second, contact forces acting at a distance produce torques. Finally, all other torques are termed body moments and specified per unit reference length. 5 illustrates the various torques acting on the rod.

The contact moment at a point s is defined by a three element vector $\mathbf{m}(s) \in \square^3$. Consider a deformed segment of the rod from c to s as shown in Figure 2.5. The rod experiences internal moments at points c and s. The rod also experiences a torque produced by the contact forces $\mathbf{n}(s)$ and $\mathbf{n}(c)$ acting at a distance $\mathbf{r}(s)$ and$\mathbf{r}(c)$. The resulting moments are $\mathbf{r}(s)\times\mathbf{n}(s)$ and $\mathbf{r}(c)\times\mathbf{n}(c)$. Finally, all the other torques acting on the rod from $[c \quad s]$are termed as the body moments, measured per reference unit length and represented as $\int_c^s \left[\mathbf{r}(\xi)\times\mathbf{f}(\xi)+\mathbf{l}(\xi)\right]d\xi$. where $\mathbf{r}(\xi)\times\mathbf{f}(\xi)$is the torque produced by a distributed body force acting at a distance $\mathbf{r}(\xi)$ and $\mathbf{l}(\xi)$ is the body moment per reference length. Typically the body moment is considered to be zero.

The sum of all moments acting on the rod from c to $s$is given as

$$\mathbf{m}(s)-\mathbf{m}(c)+\mathbf{r}(s)\times\mathbf{n}(s)-\mathbf{r}(c)\times\mathbf{n}(c)=-\int_c^s \left[\mathbf{r}(\xi)\times\mathbf{f}(\xi)+\mathbf{l}(\xi)\right]d\xi, \qquad (2.11)$$

where $\mathbf{m}(s)$and $\mathbf{m}(c)$are the contact moments at c and $s$and torques produced by the contact forces acting at a distance are given by $\mathbf{r}(s)\times\mathbf{n}(s)$, $-\mathbf{r}(c)\times\mathbf{n}(c)$ noting that the sign convention remains the same as that used in the force balance equation. Finally, the

sum of all the external moments acting on the rod is given by $\int_c^s \left[\mathbf{r}(\xi)\times\mathbf{f}(\xi)+\mathbf{l}(\xi)\right]d\xi$. Differentiating (2.10) with respect to s, $\dot{\mathbf{m}}+\dot{\mathbf{r}}\times\mathbf{n}=\mathbf{0}$.

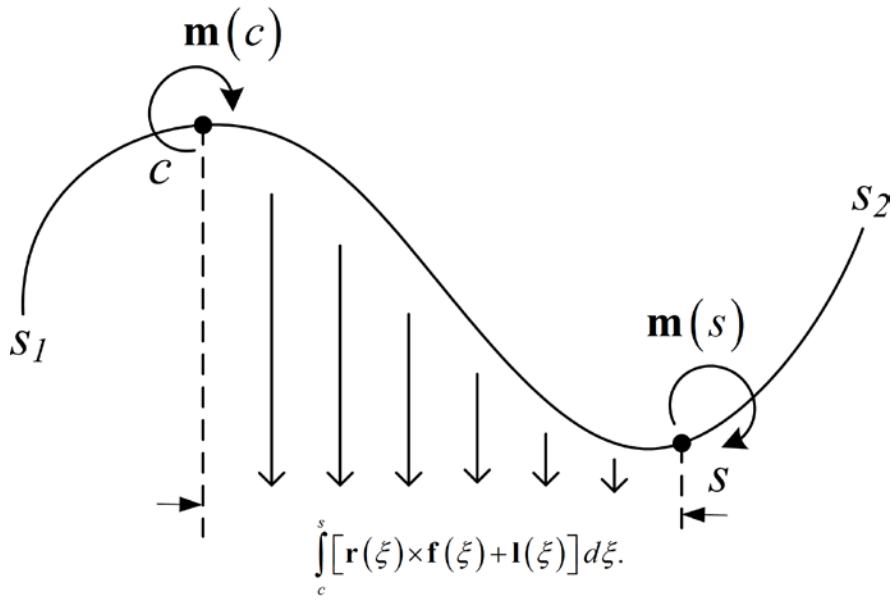

Figure 2.5 An illustration of moment balance equation on a rod from c to s. Contact moments $\mathbf{m}(c)$ and $\mathbf{m}(s)$ are produced by the internal moments. External contact moments other than contact forces acting on the rod between $[c \quad s]$ are given by $\int_c^s \left[\mathbf{r}(\xi)\times\mathbf{f}(\xi)+\mathbf{l}(\xi)\right]d\xi$.

2.7.4 Constitutive equation

The internal moments acting on a rod can be related to the local angular bending velocities using the constitutive equations. The relation between the resultant internal moments at any arbitrary point s and the angular bending velocities in global coordinates is given by

$$\mathbf{m}(s)=\mathbf{R}(s)\mathbf{C}\mathbf{u}^{l}(s), \tag{2.12}$$

where $\mathbf{R}(s)$ is the rotation matrix which maps between the local to global frame and $\mathbf{C}$ is a material constant given by $\mathbf{C}=diag\left[C_1 \quad C_2 \quad C_3\right]$. In particular, $C_1=EI_1$, $C_2=EI_2$ and

$C_3 = GJ$ where E is the modulus of elasticity, I_1, I_2 are the first moment of inertia about the local *x* and *y* axis, G is the shear modulus, and J is the polar moment of inertia. Differentiating the above equation, $\dot{\mathbf{m}} = \mathbf{R}\hat{\mathbf{u}}^l\mathbf{C}\mathbf{u}^l + \mathbf{R}\mathbf{C}\dot{\mathbf{u}}^l$. where $\hat{\mathbf{u}}^l$ is the skew symmetric matrix defined.

Substituting the result from constitutive equation into the moment balance equation and solving for $\dot{\mathbf{u}}^l(s)$,

$$\dot{\mathbf{u}}^l(s) = -\mathbf{C}^{-1}\left[\hat{\mathbf{v}}^l\mathbf{R}^{\mathrm{T}}\left[\mathbf{v}_{tip} + \rho Ag\left(s_{tip} - c\right)\mathbf{e}_g\right] + \hat{\mathbf{u}}^l\mathbf{C}\mathbf{u}^l\right] \tag{2.13}$$

2.7.5 Final ODE

The shape of the rod can be computed by integrating the above equations, simultaneously. This concludes the derivation of 3D statics of a single section continuum robot. The next chapter provides the extension of the derivation to multiple sections. The final integration inputs for the ODE solver are, $\dot{\mathbf{r}}(s) = \mathbf{R}(s)\mathbf{v}^l(s)$, $\dot{\mathbf{R}}(s) = \mathbf{R}(s)\hat{\mathbf{u}}^l(s)$, $\&, \dot{\mathbf{u}}^l(s) = -\mathbf{C}^{-1}\left[\hat{\mathbf{v}}^l\mathbf{R}^{\mathrm{T}}\left[\mathbf{v}_{tip} + \rho Ag\left(s_{tip} - c\right)\mathbf{e}_g\right] + \hat{\mathbf{u}}^l\mathbf{C}\mathbf{u}^l\right]$, where $\mathbf{v}^l(s) = \mathbf{D}^{-1}\mathbf{R}^{\mathrm{T}}\left[\mathbf{v}_{tip} + \rho Ag\left(s_{tip} - c\right)\mathbf{e}_g\right] + \mathbf{e}_e$.

2.8 Conclusion

Continuum robots are a type of biologically inspired robot built on a flexible continuous backbone. The structure of these robots looks similar to the biological structures such as an octopus arm or an elephant trunk. Due to the flexibility of continuum robots, they can be used in cluttered and congested environments. Describing the shape of a continuum robot has been a challenge for many years. The shape predicted by the widely used constant curvature model lacks accuracy because of the exclusion of gravity loading. Alternately, Cosserat rod theory describes the shape of the continuum

robot by accounting for gravity. This chapter presented the necessary equations which contribute to the deformations of the rod for a single section continuum model. The analysis is performed in three steps: the Initial and Boundary Conditions, Kinematics, and Mechanics. This model lays a foundation for the multi-section model discussed in the next chapter.

CHAPTER III

TWO-DIMENSONAL STATICS OF A MIULTI-SECTION CONTINUUM ROBOT

3.1 Introduction

As discussed previously, accessibility is defined as the ability of a continuum trunk to reach a particular location in its workspace. The accessibility of a continuum trunk can be enhanced by using a multiple section continuum robot. A serially cascaded single section continuum robot forms a multiple section continuum trunk. While there are many snake-like structures with a single section backbone proposed for performing complex medical surgeries [28, 32], for applications such as grasping [22] or working in constrained and unstructured environments, multi-section structures prove to be useful [22, 25, 27, 30].

This chapter is divided in two parts. The first part of the chapter extends the single section statics model discussed in [18] to encompass multiple sections by defining the changes occurring in the connecting region between each section; this area is termed the section transition. The second part presents the foundations for a cable-actuated robot by studying the deformations due to the addition of cable guides on the single section model. Cable guides are circular disks which support cables which run along the length of the backbone. The verification of both multi-section statics and single-section statics including cable guides is presented in the next chapter.

3.2 Background

Various prototypes built on the most widely used constant curvature model demonstrate impressive abilities in grasping geometric objects while maintaining stability [22], grasping long wooden pieces [25], in whole arm manipulation [33], when employed as an active cannula [14], and in many other applications [17]. However, since these models exclude the effects of gravity, the predicted versus the actual shape and tip location of these robots are inaccurate.

This lack of accuracy can be enhanced by modeling multiple section continuum robots using a more comprehensive approach based on Cosserat rod theory. For example, an active cannula [14, 15, 20] modeled using this approach was extended to encompass multiple sections. Although this approach demonstrated accurate predictions with an average error of 0.61% in predicting the tip location of the robot, the model is confined to a specific type of robot. A geometrically exact continuum robot with three sections also modeled on the basis of Cosserat rod theory presented less than five percent accuracy in the average tip position error in actual versus observed Cartesian tip location [30]. But the model applies specifically to the Oct-Arm robot. Hence there is a need for a multi-section model which can provide accessibility with accuracy and also be generic

3.3 Multi-Section Statics of a Continuum Robot Overview

The 3D static analysis begins by defining a section transition for a multi-section continuum robot; the analysis is then sub-divided in three sections: kinematics, mechanics and initial and boundary conditions. For simplicity, the static analysis is applied to only two- sections; however, the analysis is extendable to an n-section continuum model.

3.3.1 Section transition

The connecting region between two single sections is defined as a section transition. The section transition is assumed to be smooth and continuous. In other words, there is no hinge, no additional links to join both sections, and no shocks. The section transition treated as a discontinuity and the necessary boundary conditions are derived; however it is assumed of zero length, though this assumption can easily be relaxed by adding an arbitrary offset. The shape of the rod is now subject to external, internal forces and torques observed at each section as shown in Figure 3.1.

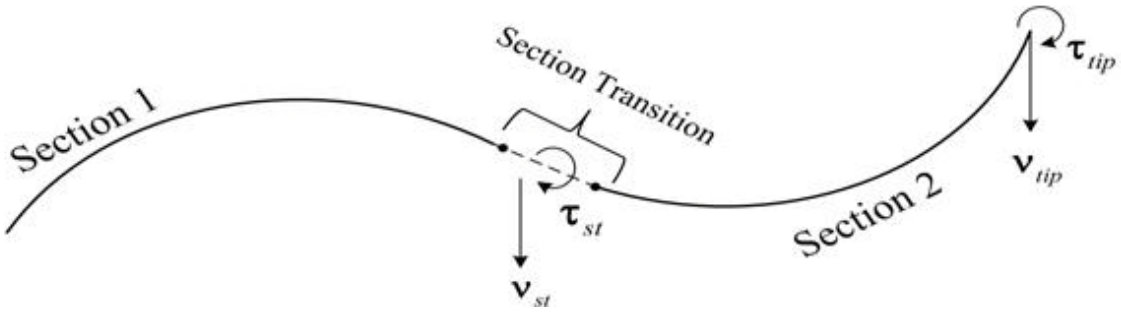

Figure 3.1 A 2D view of a two-section continuum model with the section transition shown as dotted line. Here, τ_{st}, ν_{st} are the external tip torque and force at the section transition and τ_{tip}, ν_{tip} are the external tip torque and force at the tip of section two. The section transition is assumed to be of zero length.

3.4 Multi-section kinematics

Kinematics determines the orientation and position along any point on the rod. The objective is to obtain the initial position and orientation of the second section based on the known position and orientation of the first section combined with effects produced by the section transition. The following notation is used throughout the derivation: s^+ signifies the beginning of the second section and s^- the end of first section as shown in Figure 3.2

The position and orientation along any point on the rod for a single section are given by $\dot{\mathbf{r}}(s) = \mathbf{R}(s)\mathbf{v}^l(s)$ and, $\dot{\mathbf{R}}(s) = \mathbf{R}(s)\hat{\mathbf{u}}^l(s)$, where $\mathbf{v}^l(s)$ is gives the shear strains, $\mathbf{R}(s)$is a rotation matrix specifying the orientation of the backbone, and $\hat{\mathbf{u}}^l$ is a skew symmetric matrix containing spatial bending velocities. Hence, at the end of section one the position and the orientation of the rod are represented by $\mathbf{r}(s^-)$and $\mathbf{R}(s^-)$ where s^-signifies the end of first section.

By the earlier assumptions, the position and orientation at the beginning of the second section match the position and orientation of the end of the first section are therefore given by

$$\mathbf{r}(s^-) = \mathbf{r}(s^+) \tag{3.1}$$

$$\mathbf{R}(s^-) = \mathbf{R}(s^+). \tag{3.2}$$

3.5 Multi-section mechanics

The mechanics section describes the deformations of the rod when subject to resultant forces and torques coupled with constitutive equations and kinematics. This section is divided in two sections: force balance and moment balance. The objective of the force balance equation is to determine the shear strains $\mathbf{v}^l(s)$ for a multi-section configuration. The force balance equation sums all the forces acting on the rod, which includes a known force at the section transition. Similarly, the objective of the moment balance equation for a multi-section robot is to determine the initial bending $\mathbf{u}^l(s^+)$of section two. The moment balance sums all the torques acting on the rod, which includes a known torque at the section transition.

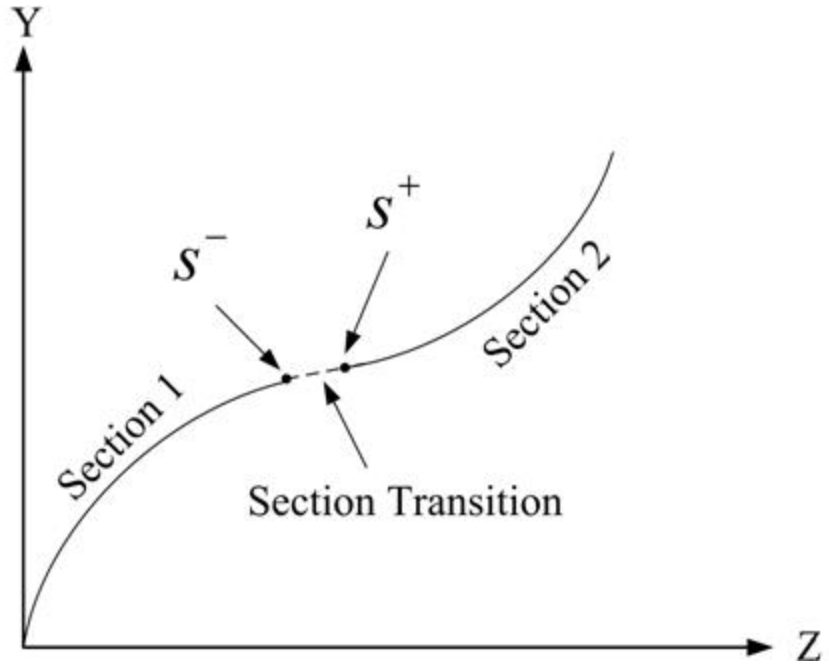

Figure 3.2 A two-section continuum model in a bent configuration with the section transition. Although the section transition is of zero length, for illustration purposes it is denoted as a dotted line. By definition, the end of one section is the beginning of the second section. The symbol s^+ denotes the beginning of the second section while s^- denotes the end of section one.

3.5.1 Force balance equation

Three types of force act on the rod: first, point forces consists of the tip force $\mathbf{v}_{tip}$ and the section transition force $\mathbf{v}_{st}$. The point force at the location of the section transition s^{st} is mathematically represented with the help of a unit impulse function $\delta(s)$ and is given by $\mathbf{v}_{st}\delta(s^{st})$ where $\delta(s^{st})$. Second, a contact force $\mathbf{n}(s)$ due to the elastic nature of the backbone as discussed in chapter 2 shapes the rod. Finally, body forces represented by $\mathbf{f}(s)$ must be included. Figure 3.3 illustrates various forces on the rod.

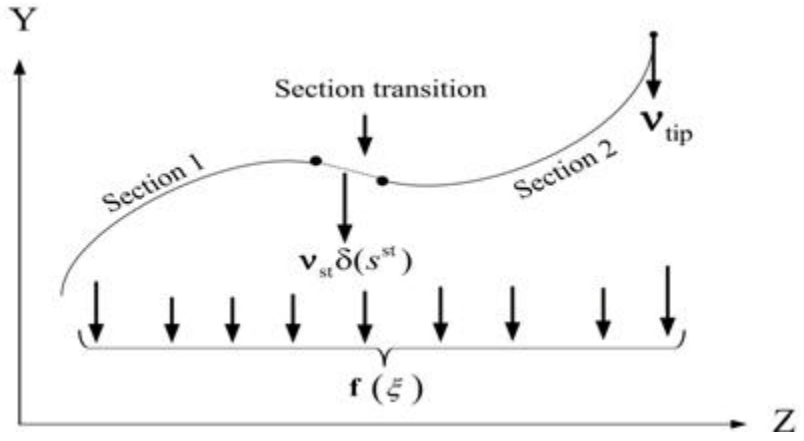

Figure 3.3 This diagram depicts some of the forces present on two-section robot. The external tip force is given by $\mathbf{v}_{\text{tip}}$, the external force at the section transition is given by $\mathbf{v}_{\text{st}}\delta\left(s^{st}\right)$ and the body force per unit length is given by $\mathbf{f}(s)$.

By picking an arbitrary point c in the first section and s on the second section, the force balance equation is given by $\mathbf{n}(s)-\mathbf{n}(c)+\int_c^s\left(\mathbf{v}_{\text{st}}\delta\left(\xi-s^{\text{st}}\right)+\mathbf{f}(\xi)\right)d\xi=\mathbf{0}$, where $\mathbf{n}(s)$ is the contact force at some arbitrary point in section two, $\mathbf{n}(c)$ is the contact force at some arbitrary point in section one, and $\mathbf{v}_{\text{st}}\delta\left(\xi-s^{\text{st}}\right)$ is the external force if present at the section transition, and the body force is $\mathbf{f}(\xi)$.

Replacing s with s^{tip}, the unstretched length of the rod, allows inclusion of the force present at the tip of the rod. Rewriting the force balance equation, $\mathbf{n}\left(s^{tip}\right)-\mathbf{n}(c)+\int_c^{s^{tip}}\left(\mathbf{v}_{\text{st}}\delta\left(\xi-s^{\text{st}}\right)+\mathbf{f}(\xi)\right)d\xi=\mathbf{0}$. Replacing $\mathbf{n}\left(s^{tip}\right)$ with $\mathbf{v}_{\text{tip}}$ and recalling the sifting property of the delta function, $\int_c^s\mathbf{v}_{\text{st}}\delta\left(\xi-s^{\text{st}}\right)d\xi=\mathbf{v}_{\text{st}}$. Therefore, $\mathbf{v}_{\text{tip}}-\mathbf{n}(c)+\mathbf{v}_{\text{st}}+\int_c^{s^{tip}}\mathbf{f}(\xi)d\xi=\mathbf{0}.$

Solving for $\mathbf{n}(c)$ and computing the integral of the body force for a constant rod density and cross-sectional area, $\mathbf{n}(c)=\mathbf{v}_{\text{tip}}+\mathbf{v}_{\text{st}}+\rho Ag\left(s^{tip}-c\right)\mathbf{e}_g$.

3.5.2 Constitutive equation

From the linear constitutive relationship as discussed in of the previous chapter, $\mathbf{n}(s) = \mathbf{RD}\left(\mathbf{v}^{l}(s) - \mathbf{e}_{\mathbf{e}}\right)$. By substituting in the above equation and solving for $\mathbf{v}^{l}(s)$, the local shear strains along any point on the rod can be analytically computed by $\mathbf{v}^{l}(s) = \mathbf{D}^{-1}\mathbf{R}^{\mathrm{T}}\left(\mathbf{v}_{\mathrm{tip}} + \mathbf{v}_{\mathrm{st}} + \rho Ag\left(s^{tip} - s\right)\mathbf{e}_{g}\right) + \mathbf{e}_{e}$. Note that the analytical computation begins at s^{tip} and proceeds backwards to the desired location on the trunk. When the portion of the rod $\left(s, s^{tip}\right)$ does not include the section transition, the equation for $\mathbf{v}^{l}$ must reflect its lack. The following Table 3.1 summarizes the shear strain equation where s^{st} is the location of the section transition on the rod.

Table 3.1 Shear strain equations for a multi-section model

$\mathbf{v}^{l}(c) = \mathbf{D}^{-1}\mathbf{R}^{\mathrm{T}}\left(\mathbf{v}_{\mathrm{tip}} + \mathbf{v}_{\mathrm{st}} + \rho Ag\left(s^{tip} - c\right)\mathbf{e}_{g}\right) + \mathbf{e}_{e}$	If $s < s^{st}$
$\mathbf{v}^{l}(c) = \mathbf{D}^{-1}\mathbf{R}^{\mathrm{T}}\left(\mathbf{v}_{\mathrm{tip}} + \rho Ag\left(s^{tip} - c\right)\mathbf{e}_{g}\right) + \mathbf{e}_{e}$	If $s > s^{st}$

3.5.3 Moment balance at section transition

There are three types of torques present at the section transition. They are the contact moments $\mathbf{m}(s)$ as defined in the previous chapter, the torques produced by the contact forces $\mathbf{n}(s)$ acting at a distance $\mathbf{r}(s)$, and point torques. The point torques consist of the applied external point torque $\boldsymbol{\tau}_{st}$ at the section transition which is represented with the help of a unit impulse function as defined in the force balance section, and the torque produced by the point force $\mathbf{v}_{st}$ at the section transition. The initial bending strain $\mathbf{u}^{l}\left(s^{+}\right)$ for section two can be obtained from $\mathbf{m}\left(s^{+}\right)$, the contact couple observed at s^{+}, which can be obtained with the help of the moment balance equation.

By replacing c with s^{-} and s with s^{+} in the moment balance equation (2.10) from chapter two,

$$\mathbf{m}(s^+)-\mathbf{m}(s^-)-\mathbf{r}(s^-)\times\mathbf{n}(s^-)+\mathbf{r}(s^+)\times\mathbf{n}(s^+)+\int_{s^-}^{s^+}\left(\mathbf{r}(s^+)\times\mathbf{v}_{\mathrm{st}}\delta(\xi-s^{st})+\boldsymbol{\tau}_{\mathrm{st}}\delta(\xi-s^{st})\right)d\xi=\mathbf{0},$$

where $\mathbf{m}\left(s^+\right)$ and$\mathbf{m}\left(s^-\right)$ are the bending moments produced at the section transition while$\mathbf{r}(s^-)\times\mathbf{n}(s^-)$ and $\mathbf{r}(s^+)\times\mathbf{n}(s^+)$ are the contact torques produced by the contact forces and$\mathbf{n}\left(s^+\right)$ at s^+ and s^-. Finally, the integral $\int_{s^-}^{s^+}\left(\mathbf{r}(s^+)\times\mathbf{v}_{\mathrm{st}}\delta(\xi-s^{st})+\boldsymbol{\tau}_{\mathrm{st}}\delta(\xi-s^{st})\right)d\xi$ is the resultant of all other torques experienced by the rod other than internal torques. Specifically, $\mathbf{r}(s^+)\times\mathbf{v}_{\mathrm{st}}\delta(\xi-s^{st})$ is the torque produced due to external force present at the section transition acting at $\mathbf{r}\left(s^+\right)$ and $\boldsymbol{\tau}_{\mathrm{st}}\delta(s^{st})$ is the body couple applied to the section two.

Since the position $\mathbf{r}\left(s^-\right)=\mathbf{r}\left(s^+\right)$for consistency, $\mathbf{r}\left(s^+\right)$is used. The above equation is reduced as follows:

$$\mathbf{m}(s^+)-\mathbf{m}(s^-)+\mathbf{r}(s^+)\times\mathbf{n}(s^+)-\mathbf{r}(s^+)\times\mathbf{n}(s^-)+\mathbf{r}(s^+)\times\mathbf{v}_{\mathrm{st}}+\boldsymbol{\tau}_{\mathrm{st}}=0.$$

$$\mathbf{m}(s^+)-\mathbf{m}(s^-)+\mathbf{r}(s^+)\times\left[\mathbf{n}(s^+)-\mathbf{n}(s^-)+\mathbf{v}_{\mathrm{st}}\right]+\boldsymbol{\tau}_{\mathrm{st}}=0. \tag{3.3}$$

From(2.5), $\mathbf{n}(s^+)-\mathbf{n}(s^-)+\int_{s^+}^{s^-}\mathbf{v}_{\mathrm{st}}\delta\left(\xi-s^{st}\right)d\xi=\mathbf{0}$, so $\mathbf{n}(s^-)=\mathbf{n}(s^+)+\mathbf{v}_{\mathrm{st}}$.

Substituting $\mathbf{n}\left(s^-\right)$ in (3.3), $\mathbf{m}(s^+)=\mathbf{m}(s^-)-\boldsymbol{\tau}_{\mathrm{st}}$. Noting that $\mathbf{m}\left(s^+\right)$ and $\mathbf{m}\left(s^-\right)$ can be replaced by their constitutive equations in global coordinates, $\mathbf{m}\left(s^+\right)=\mathbf{R}\left(s^+\right)\mathbf{C}\mathbf{u}^l\left(s^+\right)$ and $\mathbf{m}\left(s^-\right)=\mathbf{R}\left(s^-\right)\mathbf{C}\mathbf{u}^l\left(s^-\right)$. The above equation is reduced to, $\mathbf{R}\left(s^+\right)\mathbf{C}\mathbf{u}^l\left(s^+\right)=\mathbf{R}\left(s^+\right)\mathbf{C}\mathbf{u}^l\left(s^-\right)-\boldsymbol{\tau}_{\mathrm{st}}$ and $\mathbf{u}^l\left(s^+\right)=\mathbf{u}^l\left(s^-\right)-\mathbf{C}^{-1}\mathbf{R}\left(s^+\right)^{\mathrm{T}}\boldsymbol{\tau}_{\mathrm{st}}$.The following summarizes the necessary equations which defined the shape of the rod at the beginning section two, given the shape at the end of section one and a known force and torque applied to the section transition $\mathbf{r}\left(s^+\right)=\mathbf{r}\left(s^-\right)$, $\mathbf{R}\left(s^+\right)=\mathbf{R}\left(s^-\right)$& $\mathbf{u}^l\left(s^+\right)=\mathbf{u}^l\left(s^-\right)-\mathbf{C}^{-1}\mathbf{R}\left(s^+\right)^{\mathrm{T}}\boldsymbol{\tau}_{\mathrm{st}}$. This concludes the derivation for the multi-section statics of a two-section continuum robot. The next chapter introduces a test bench which validates the multi-section model. The next section discusses the effects of cable guide mass on a single section continuum model.

3.6 Robotics applications of Cosserat rod theory

Cable guides are essential for routing the cables to pass along the length of the rod. However, these cable guides add additional weight along the length of the rod as illustrated in Figure 4. The equations which describe the model should be adjusted to account for the additional mass and compute the overall shape. This has been implemented in two different ways.

The first approach, termed the average mass model, takes the combined mass of the rod with the cable guides into a single overall density of the rod rather than specifically placing the mass of each cable guide at the specific locations. In contrast, the second approach accurately models the change in the density and the cross sectional area due to the presence or absence of each cable guide. This approach is named the accurate mass model.

Mechanical details such as size, dimensions, and material properties of the cable guide and the rod, along with the experimental results, are presented in the next chapter. This section focuses on how the Cosserat rod equations are modified by the addition of cable guides using the above mentioned methods.

3.7 Average mass model

The average mass method provides one approach to incorporate this additional weight produced by the cable guide. The body force at a particular point s given by $\mathbf{f}(s) = \rho A g(s)\mathbf{e}_\mathbf{g}$, where ρ is the density, A is the cross sectional area of the material, and g is the acceleration due to gravity. The only parameter which varies when compared to a rod with no cable guides is the averaged density of the rod and cable guides ρ.

The local shear strains contained in $\mathbf{v}'(s)$ is the only equation which changes because it contains the density of the material ρ. Specifically, the new average density is

given by $\rho_{avg} = \frac{m_r + m_{cg}}{r_l}$, where m_r is the mass of the rod, m_{cg} is the mass of the cable guide and r_l is the length of the rod. The revised body force is then computed using this new average density ρ_{avg}. Experimental results resulting from this approach are presented in the next chapter.

3.8 Accurate mass model

As seen in the average mass method, local shears $\mathbf{v}^l(s)$ must be adjusted to add the additional weight produced by the cable guides. The accurate mass method accurately reflects the changing density ρ and cross-sectional area A due to the presence or absence of cable guides at each point along the rod.

As the cable guides are spaced out evenly along the rod and have a specific volume, the effective density of the rod with the cable guide should be employed only at those locations where the cable guide is present. The analysis is divided into two sections. The first section shows the calculation of the effective density of the rod combined with the cable guide. The second section provides a method to determine the total length of the portion of the rod which contains cable guides between a given point on the rod and the tip of the rod.

The effective density ρ_e is calculated as $\rho_e = \frac{m_{cg} + \left(\frac{m_r h_{cg}}{r_l}\right)}{V_{cg}}$, where m_{cg} is the mass of the cable guide, m_r mass of the rod, h_{cg} is the thickness of the cable guide, r_l is the unstretched length of the rod, and V_{cg} is the volume of the cable guide. The effective density is specifically reflected in the force balance equation. For all the locations on rod where the cable guide is present the effective density ρ_e is used instead of ρ, the density of the rod.

For the locations on the portions of the rod which do not contain a cable guide, the body force is given by $\mathbf{f}(s) = \rho A g(s)\mathbf{e}_\mathbf{g}$ where s is an arbitrary point on the rod, ρ is the density of the material, and A is the cross sectional area of the rod. For all the locations on the rod which contain a cable guide, the effective density ρ_e and the cross sectional A_{cg} of the cable guide are used.

$$\mathbf{f}(s) = \begin{cases} \rho A g(s)\mathbf{e}_g & s \text{ in rod} \\ \rho_e A_{cg} g(s)\mathbf{e}_g & s \text{ in cable guide} \end{cases}$$

With the effective densities calculated, the next step is to compute the total length of the portion of the rod which contains cable guides between a given point on the rod and the tip of the rod. To determine this, the backbone is divided into four sections: offset, end-effector region, cable guide, and rod. 5 shows a side view of a thin rod mounted along the *z* axis, with cable guides uniformly separated. For simplicity of illustration, the rod is in a zero gravity environment; as a result, the sag due to gravity is not shown.

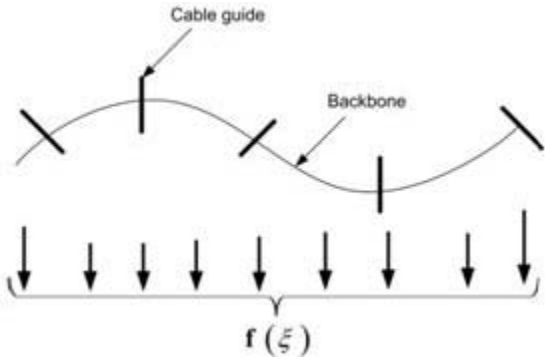

Figure 3.4 A 2D view of a single section continuum backbone with a set of circular

Offset is the length of the rod measured from $s = 0$ to the beginning of the first cable guide; this length is defined as o. Length y defines the length of the end-effector-

region, which is measured from the tip of the rod s_f to the last cable guide. From earlier, h_{cg} is the thickness of the cable guide. Since the cable guides are equally spaced, the cable guide spacing is a periodic value which is represented by G and is given by $G = \alpha + h_{cg}$ where α defines the distance between the cable guides. There are four cases to consider in implementing the accurate mass model. Thebody force function $\mathbf{f}(s)$ varies depending on the position s on the rod. In particular, there are four cases. In the first case, s lies within the offset, in the second s lies in the end effector region, in the third it lies on the rod where a cable guide is absent, and in fourth it lies on the cable guide as shown in Figure 3.5. The next section determines how the body force function varies in the above mentioned cases.

If the current location s is in the offset region, then the total length of portion of the rod under consideration which contains cable guides is given by Nh_{cg} where N is the number of cable guides and the body force equation is given by

$$\mathbf{f}(s) = \rho A g \mathbf{e}_g \left((N-1)\alpha + y + (o - s) \right) + \rho_e A_{cg} g \mathbf{e}_g \left(N h_{cg} \right)$$

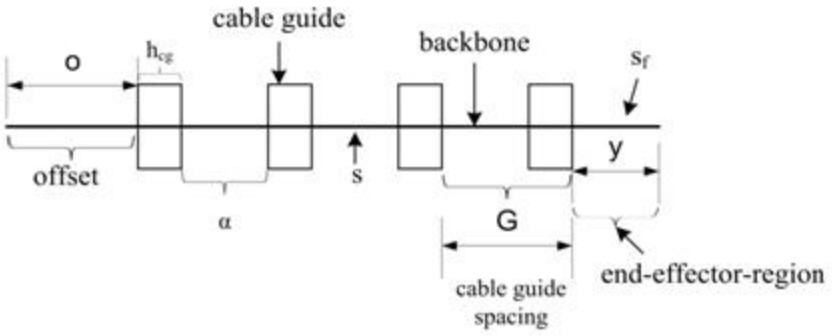

Figure 3.5 This diagram depicts a side view of a thin rod with cable guides. The various regions of the rod are also shown.

If the current location s is in the end-effector region, then the total length of the cable guides is zero and the body force equation is given by $\mathbf{f}(s) = \rho A g \mathbf{e}_g \left(s_f - s \right)$.If the

current location is not on the offset or in the end effector region then it either lies at a point on the rod where no cable guide is present or a point where there is a cable guide. Therefore a modulus operator can be used to break the rod into a serious of sections, where each of the sections consists of a cable guide and rod. Also, the modulus operator is used to determine whether the point lies in the cable guide portion of the section or if it lies within the rod portion of the section, then compute the desired body force. The mod operator is used as follows: $r = \mathrm{mod}\left(s_f - y - s, G\right)$.The mod operator returns a reminder, which is compared with a set of predefined values which are specific to the dimensions of the cable guide and the rod as shown in Figure 3.6.

If the remainder r from the mod operator lies between n_1 and n_2, then the chosen point s lies within a cable guide. Therefore the total length of the portion of the rod under consideration which contains cable guides, abbreviated c_{gl}, is given by

$$c_{gl} = \left\lfloor \left(\frac{s_f - y - s}{G} \right) \right\rfloor h_{cg} + r$$

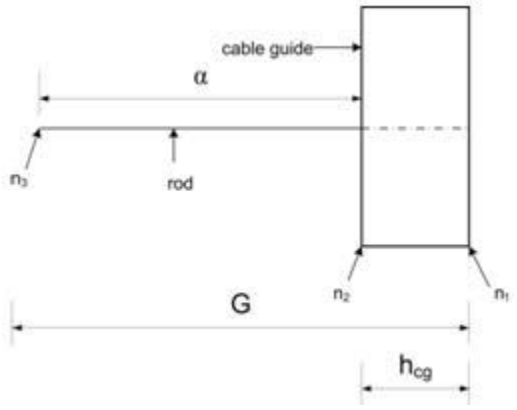

Figure 3.6 A section of cable guide and rod. The n_1, n_2, and n_3 points are the predetermined reminder values which are specific to the dimensions of the cable guide and the rod.

The total length of the portion of rod under consideration which does not contain cable guides, termed rod length r_l, is given by $r_l = s_f - s - c_{gl}$. The body force for the all the points inside the cable guide is given by

$$\mathbf{f}(s) = \rho A g \mathbf{e}_g r_l + \rho_e A_{cg} g \mathbf{e}_g c_{gl} \tag{3.4}$$

If the returned value from the mod operator lies between n_2 and n_3, then the point lies within the rod but not within the cable guide. Therefore length of rod r_l which does not contain a cable guide, measured from the end of the rod till the current location of s, is given by $r_l = \left\lfloor \left(\frac{s_f - y - s}{G} \right) \right\rfloor \alpha + r$ and the length of the rod containing cable guides c_{gl} is given by $c_{gl} = s_f - s - r_l$. The body force for the all the points on the rod is again given by (3.4).

In conclusion, Table 3.2 summarizes the various body force equations. The experimental results of the effects of cable guide mass, determined by comparing the predicted versus the actual tip locations, for both the average and accurate mass models are presented in the next chapter.

Table 3.2 Body force equations for accurate mass model

$\mathbf{f}(s) = \rho A g \mathbf{e}_g \left((N-1)\alpha + y + (o-s) \right) + \rho_e A_{cg} g \mathbf{e}_g \left(N h_{cg} \right)$	If s is in the offset
$\mathbf{f}(s) = \rho A g \mathbf{e}_g \left(s_f - s \right)$	If s is in the end-effector region
$\mathbf{f}(s) = \rho A g \mathbf{e}_g (r_l) + \rho_e A_{cg} g \mathbf{e}_g (c_{gl})$ $\begin{cases} n_1 \le r \le n_2 \text{ in cable guide; } c_{gl} = \left\lfloor \left(\frac{s_f - y - s}{G} \right) \right\rfloor h_{cg} + r,\ r_l = s_f - s - c_{gl} \\ n_2 \le r \le n_3 \text{ in rod; } r_l = \left\lfloor \left(\frac{s_f - y - s}{G} \right) \right\rfloor \alpha + r,\ c_{gl} = s_f - s - r_l \end{cases}$	

3.8.1 Shaping robot using cable guides

For all cable-actuated robots, it is essential to have a set of cable guides along the length of the rod separated by a fixed distance. These cable guides provide a means to route the cables along the rod. By controlling the length of the cables, the shape of the robot can be changed. Hence, cable lengths act as a valuable source for determining the shape of the robot, rather than requiring measurement of tip force and torque to determine the robot's shape.

The length of each of the three cables for a given tip loading is derived for a single-section continuum manipulator with circular cable guides in the following paragraphs. Consider a single cable guide. Assume a set of three cables separated at 120° intervals as shown in 8 run the length of the rod. The cable guide is assumed to lie in a local *yz* plane. The distance between the center of the rod to the center where the cable

passes is denoted by d. Let $\mathbf{d}^l$ be the local coordinates of the location on the cable guide where the cable passes. Since there are three cables there are three $\mathbf{d}^l_{1..3}$ Cartesian coordinates for each cable guide which are strictly local. In order to determine the shape of the robot, it is essential to convert $\mathbf{d}^l_i$ from local to global coordinates.

The global locations of the cable guides can be obtained with the help of $\mathbf{r}(s)$ and $\mathbf{R}(s)$produced by the ODE solver. The vector $\mathbf{r}(s)$ provides the global location of points on the rod at location s and $\mathbf{R}(s)$provides the orientation of the rod at that point. For ease of manipulation, the location and the orientation are represented by a homogenous transformation matrix $\mathbf{T}(s_i)=\begin{bmatrix}\mathbf{R}(s_i) & \mathbf{r}(s_i)\\ \mathbf{0} & 1\end{bmatrix}$, where $s_i$represents the location of a cable guide along the rod. The local coordinates of the cable guides are converted to global coordinates by multiplying $\mathbf{d}^l_{i,j}$ with the transformation matrix. Specifically, in global coordinates, the location of a point on the cable guide is represented by $\bar{\mathbf{d}}_{i,j}=\mathbf{T}\bar{\mathbf{d}}^l_{i,j}$, where i refers to the section index ranging from $i=1..3,$and j refers to the cable index ranging from $j=1..3.$The over-bar indicates the use of homogenous coordinates.

The sum of the distance traversed by a cable between each cable guide in global coordinates produces the calculated shape of the robot. For n cable guides, the length of the cables can be obtained by$L_{i,j}=\sum_{i=2}^{n-1}\left\|\mathbf{T}_i\mathbf{d}^l_{i,j}-\mathbf{T}_{i-1}\mathbf{d}^l_{i-1,j}\right\|$

The results of predicting the shape of the robot based on cable lengths are experimentally determined and discussed in the next chapter.

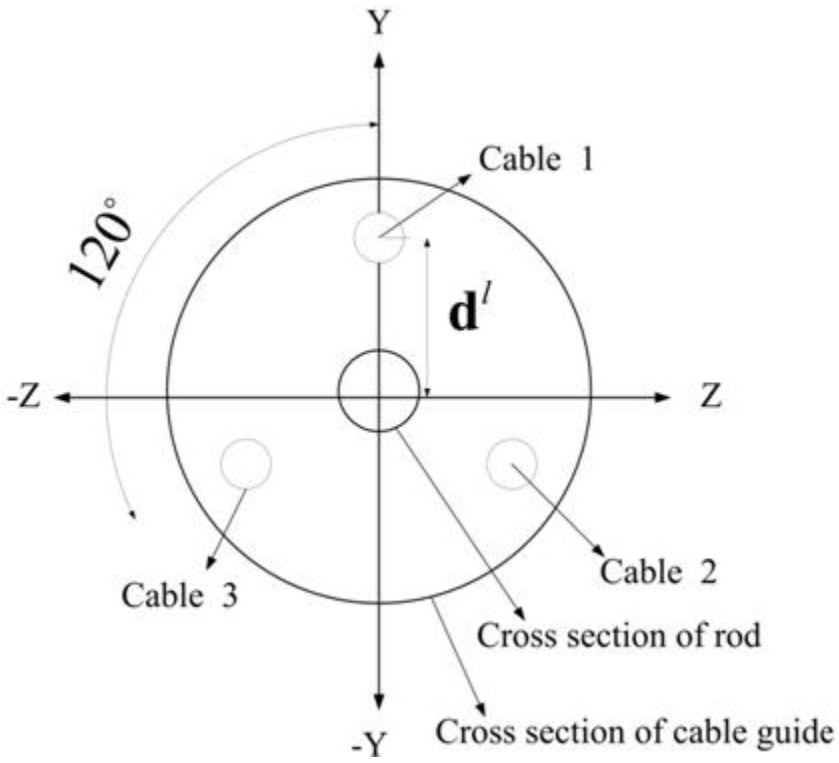

Figure 3.7 A 2D view of a cable guide. The three cables provides up to three degrees of freedom and are separated by 120°.

3.9 Conclusion

Multiple sections enhance the accessibility of a continuum robot. A model for a multi-section trunk was based on the serial connections of single sections; the region between the two sections is termed a section transition. Analysis of the section transition provides the necessary information to determine an analytical relationship between trunk shape and the end of the previous section and the beginning of the next section.

The cable-actuated design for a continuum robot provides an ideal base for rapid prototyping with low cost and complexity. For a cable-driven robot, a set cable guides separated by a known distance provide a housing for the cables to run through the length of the rod. The cable guides add significant mass which must be included in the model. This additional weight can be included using two different approaches, the average mass

model and the accurate mass model. Finally, measurement of the cable lengths provides a simple way to determine the shape of the robot. The next chapter discusses the verification setup and experiments performed to verify the effects of cable guide mass on the model, perform deflection analysis for measuring change in cable length, and validate the multi-section model.

CHAPTER IV

2D VERIFICATION OF CONTINUUM MODEL AND 2D VERIFICATION OF THE CABLE GUIDE MODEL FOR A SINGLE SECTION CONTINUUM ROBOT

4.1 Introduction

A number of potential applications of continuum robots require accuracy in placing the tip of the trunk at a desired location [7, 14]. In this thesis, the accuracy of the proposed model is defined by the difference between the Cartesian tip locations predicted by the model compared with the physical rod's tip location.

This chapter introduces two verification methods in 2D. The first section validates the multi-section model, presented in the previous chapter. The second section verifies the modeled effects of cable guide mass on the shape of the robot. Both efforts are based on the verification procedure used in [18].

4.2 Background

Various models of a multi-section continuum robot developed using Cosserat rod theory have been verified in many innovative ways. A geometrically exact model developed using Cosserat rod theory [30] was validated on the OctArm V, a three section soft robotic manipulator. OctArm consists of three sections made of rubber and equipped with pneumatic actuators as shown in Figure 4.1. The shape of OctArm is photographed under a wide range of actuator pressures and the tip positions are measured. This observed experimental data is then compared with the predicted shape and tip position [30]. The results of this verification demonstrate an average error which is less than five

percent in the tip predictions with respect to the overall length of each section. The OctArm robot also served as a verification platform for other models, including the constant curvature formulation [17]. This thesis seeks to extend the results which apply to specifically to OctArm to a wider range of cable-actuated continuum robots

Figure 4.1 OctArm manipulator [25]

The same theory was used to model an active cannula robot designed for surgical assistance. This robot, composed of pre-curved, hollow thin tubes made of a nickel-titanium alloy (Nitinol), is shown in 4.2 [31]. This robot is manually actuated and the verification bench consisted of two cameras to triangulate the location of markers placed at various points along the robot. The average tip error under load of 1.5%–3%, with respect to the overall length of the cannula for a set of experiments. However, this approach is suitable to active cannulas, but does not directly apply to modeling cable-driven continuum robots.

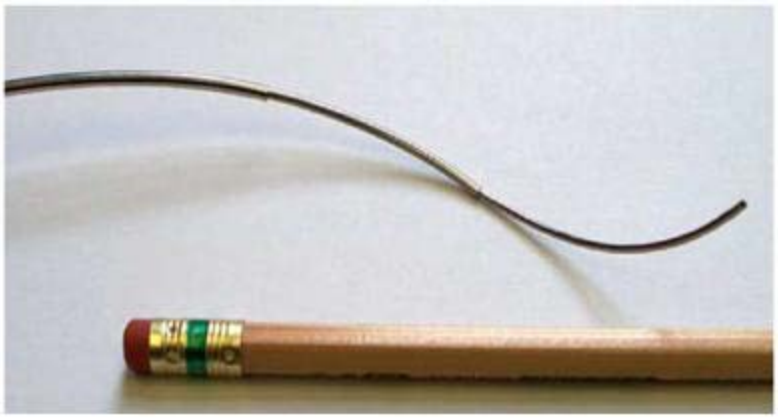

Figure 4.2 Active cannula with three sections. This robot is built using three hollow Nitinol tubes [31].

Finally, 2D verification of a 3D statics model of a single section continuum robot uses a thin rod made of a nickel-titanium alloy as the backbone [18]. The 2D verification bench primarily consists of a 45.72 cm x 60.96 cm machine etched grid with 1 mm accuracy shown in Figure 4.3. The rod is mounted on the grid and various point forces in the form of weights measured in grams is attached to the tip of the rod. The average error in predicted versus the Cartesian tip locations is 2.01% mm. The verification method adopted is generic, easy to implement and can be mounted just about anywhere without taking too much space. Although this approach is not suitable for 3D verification, this approach offers rapid verification with low cost and time. This verification setup is amenable to verify multi-section robots. Due to these advantages, this method has been used to verify the models presented in the previous chapter.

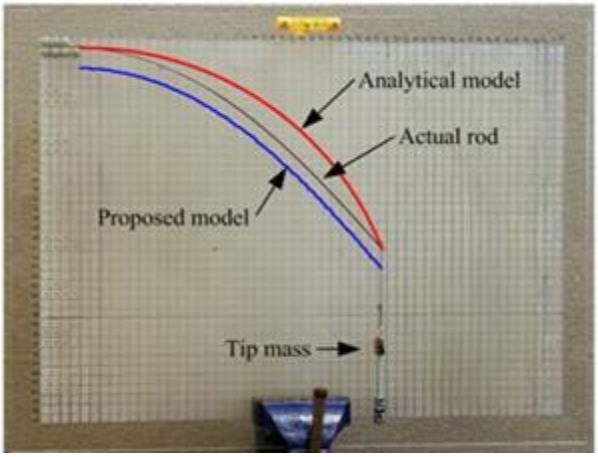

Figure 4.3 Nitinol backbone [18]

4.3 Overview

The main goal of the verification is to determine the accuracy of the models presented in the previous chapter. The 2D verification method developed in [18] is used as a base for the verification. The verification process is subdivided into a verification bench and a verification procedure. The verification bench presents the choice of material for the backbone, cable guides and other key components used when performing the experiments.

The verification procedure discusses the actual process of performing two experiments. The first experiment validates the multi-section continuum model and the second experiment verifies the effects of cable guide mass on a single-section continuum rod. Specifically, for the multi-section experiment, a set of point forces in the form of loads are attached at the tip of both sections. The various Cartesian tip locations of both sections of the rod are then recorded and compared with the predicted coordinates. Similarly, a set of cable guides are press fit onto the rod and a of series point forces in the form of loads are attached the tip of the rod. As in the previous experiment, the tip

coordinates from the rod recorded for the various loads are compared with the predicted coordinates from the model

4.4 Robot components

This section discusses the various components of the verification bench used for the experiments.

4.4.1 Backbone of the continuum robot

The backbone of the continuum robot is the most important element. The backbone must exert a restorative force and moment in response to bending and shear strains. A shape memory alloy called Nitinol, composed of nickel and titanium, was chosen as the backbone of the model.

Figure 4.4 Nitinol rod

Nitinol is being used as the backbone for many continuum models as it demonstrates a wide range of elastic deformation, allowing it to return to its original shape after bending with no permanent (plastic) deformation. Unfortunately, the modulus of elasticity for the material varies based on manufacturing properties and ambient temperature, but it is in between 45GPa-75Gpa. Figure 4.4 shows the Nitinol used for the experiments.

The rod has a diameter 1.56 mm, a length of 40 cm, and a calculated density of $6.8\frac{g}{mm^3}$. The moment of inertia for a rod with circular cross section is given by $I = \pi d^4 / 64$ and the second moment of inertia is given by $J = \pi d^4 / 32$ where d is the diameter of the rod. For the dimensions of the given rod, $I = 0.291 pm^4$ and $J = 0.581 pm^4$.

Finally, the experimentally determined values for the modulus of elasticity varied between 61.6 GPa and 62.7 GPa. The shear modulus of elasticity is given by $G = E(1+\upsilon)$ where υ is Poisson's ratio of 0.3 giving a calculated shear modulus of 20.8 GPa.

4.4.2 Cable guides and cables

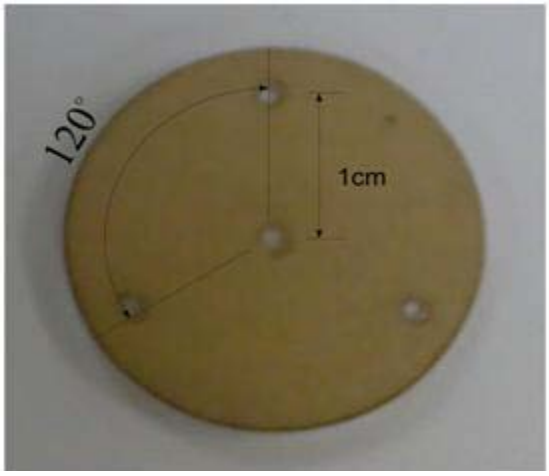

Figure 4.5 A cable guide with three holes for the cables to pass through

Cable guides serve as a support for the cables to run along the length of the rod. Circular cable guides made from acrylic are used for the experiments. The cable guides are laser cut then press fit on the Nitinol rod. Figure 4.5 shows the cable guide used in the experiments

The cable guide diameter is 5.85 mm, its thickness 3.01 mm, and its mass 2.2 grams. Five cable guides placed along the rod are separated by a ~9.5 cm center to center spacing.

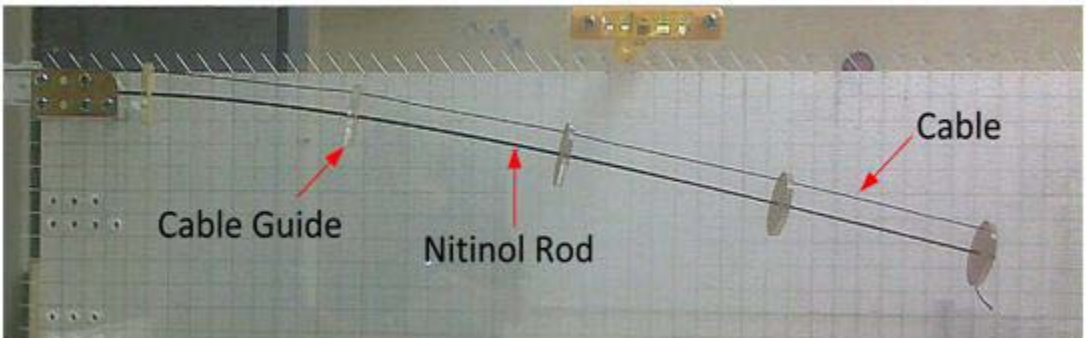

Figure 4.6 The Nitinol rod with cable and five cable guides

Three holes at 120° intervals provide an opening for the cables to pass through. The distance from the center of the cables to where cables pass is approximately 1 cm. For the cables, a special fiber cable manufactured by Dyneema was used. These cables are very strong, provide a low-friction surface, and show good tear resistance. The rod with the cable guides and a single cable is shown in Figure 4.6.

4.4.3 Grid

To accurately measure the tip locations of the rod, a flat acrylic panel is used as the reference plane as shown in Figure 4.7. The dimensions of the grid are 45.72 cmx60.96 cm; it has a 1 mm laser-etched grid. The grid is mounted on a vice with the help of two levels.

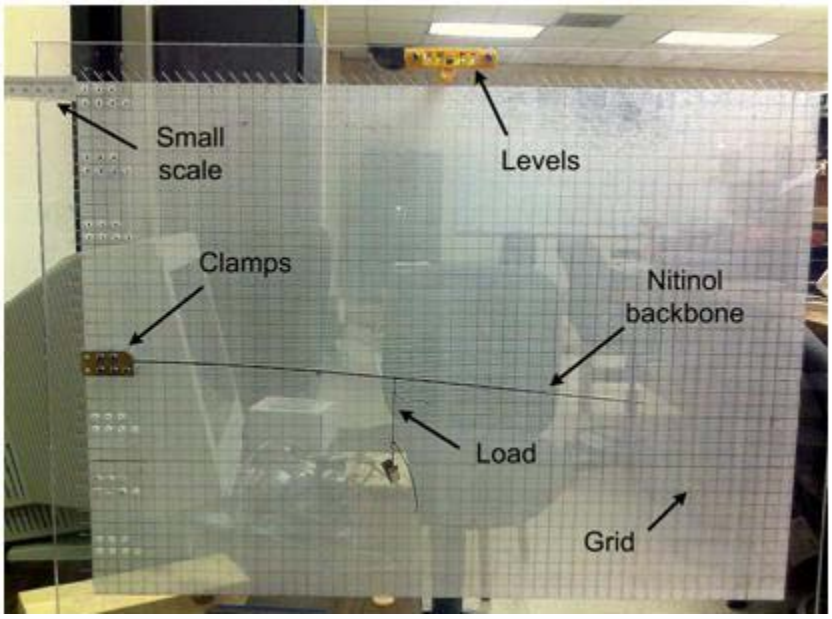

Figure 4.7 Verification setup with various components. Note the small scale refers to a small ruler of 70mm length

4.4.4 Clamps

A set of two clamps are used to firmly attach the rod to the grid. To hold the rod firmly, a 1 cm portion of the rod is securely held between two clamps as shown in Figure 4. With the help of the lower layer clamp, the mounting angle of the rod can be varied between three specific intervals, $0^\circ - 30^\circ - 60^\circ$. However, throughout the experiments the 0° mounting angle is used. The clamps are laser cut from acrylic and have a provision for six screws.

4.4.5 Levels, weights and small scale

The grid is the main element of the verification setup and a pair of two levels helps in aligning the grid vertically as shown in Figure 4.7. These levels help in eliminating out-of-plane forces due to gravity loading.

A force exerted on the tip of the robot in the form of weights was applied to the rod for the two experiments. Using a small pen scale, a set of known weights was

measured, ranging from 10 grams to 103 grams. Finally, a small ruler was used for measuring the change in the length of the cables. The ruler can measure up to 70 mm and is glued firmly to the grid as shown in Figure 4.7.

The next section explains the procedure for the two experiments.

4.5 Verification process

This section discusses the procedure for performing 2D validation of the multi-section model and of a model which includes the effects of cable guide mass. The data obtained from both experiments are compared with predicted values from the model then possible sources of errors are discussed.

In particular, the multi-section model is validated in two experiments. In the first experiment, a set of known forces in the form of calibrated masses are applied only to the end of section one while the second section has no load. For the second test, a set of two different loads are applied at the tip of both sections. Specifically, the force at section two is measured using a small pen scale, while a known tip force is applied at the end of first section. In both the tests, the tip coordinates are measured using the grid.

The effect of cable guides on the shape of a single section continuum rod is experimentally measured in the following way. The rod with five cable guides is mounted on the grid as shown in Figure 4.8. A single cable is passed through the length of the rod, terminating at the rod tip. A set of known weights are applied to the tip of the rod; similar to the previous experiment, the tip coordinates are measured using the grid. Also, with the help of a small ruler affixed to the grid, the change in the length of a reference point on the cable is also measured.

4.6 Experiment 1: 2D validation of multi-section model

The multi section model is validated with two experiments. The first experiment applies load at the end of the first section while the second section applies loads at the end of both sections. The next section describes the setup required before performing the experiments.

4.6.1 Initial setup

The grid is attached to the vise and with the help of two levels, the grid is aligned properly. The Nitinol rod is firmly attached to the grid with the help of clamps. The length of the rod is reduced by one centimeter due to clamps. For the first experiment, a load is attached at 19.5 cm of the unstretched reference length of section one, while the second section remains unloaded as shown in Figure 8(a). For the second experiment, a load is attached the end of the second section, connected by a cable of length 26.5 cm tied to a pen scale as shown in Figure 4.8(b). An addition load is placed at the end of first section.

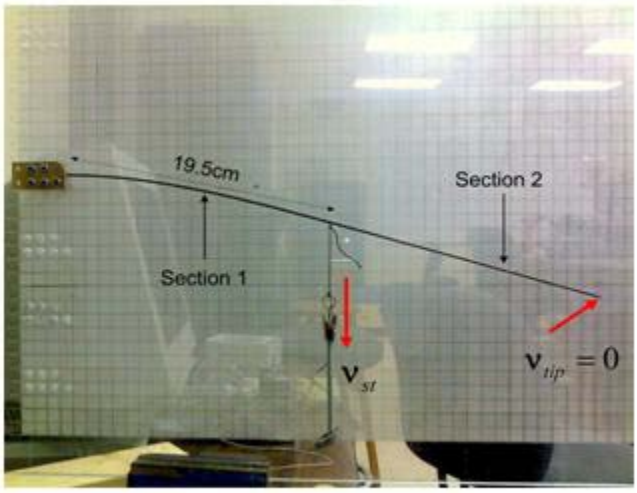

(a)

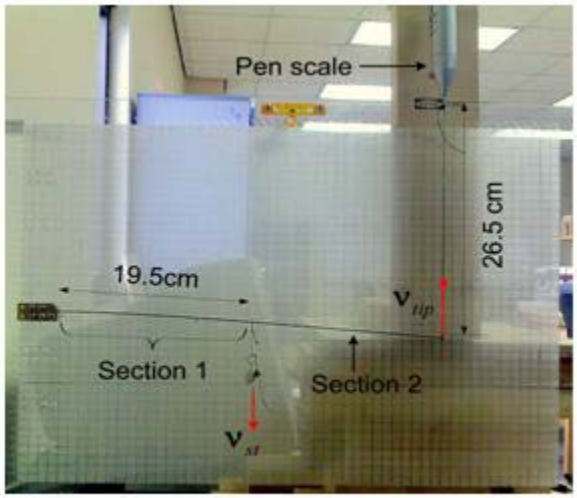

(b)

Figure 4.8 The verification setup is ready for the both the experiments. In (a) the rod is mounted on the grid and at the end of first section a point force ν_{st} in the form of a load is attached. The second section is left unloaded. In (b), both the sections are loaded. In particular, the second section is connected to a pen scale with a cable of fixed length.

4.6.2 Experimental procedure test 1a

In the first experiment a load is applied to the first section while the second section is left unloaded as shown in Figure 4.8(a). A set of five different weights ranging from 2.2 to 43 grams were measured using a pen scale and attached to the end of the

section one. For each tip load the corresponding tip coordinates of both the sections are recorded as shown in Table 9.

4.6.3 Obtaining data from model

Obtaining the data from the model begins by initializing the physical properties of rod and the initial conditions. The physical properties of the rod include: diameter, length, density and the elasticity. The initial conditions for the differential equations include initial position $\mathbf{r}(0)$, mounting angle $\mathbf{R}(0)$and the initial bending $\mathbf{u}^{l}(0)$. The next step is to enter various tip forces used in for the physical model and to record the values predicted by the model. Figure 10 shows a comparison of the shape of the physical rod with the shape predicted by the model for a -0.2059N load applied at the tip of the section.

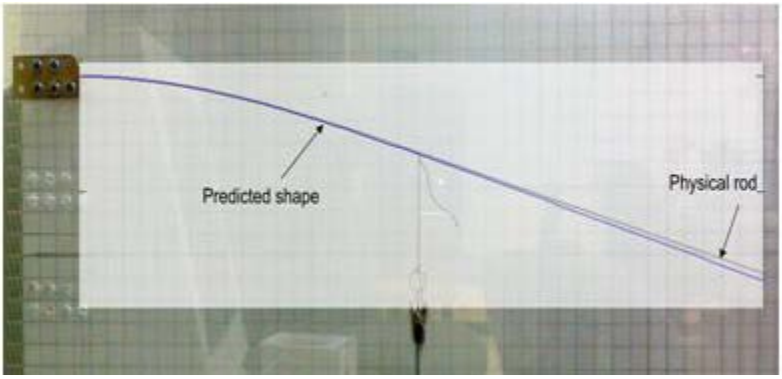

Figure 4.9 The actual and the predicted shapes of a multi section rod with a load of -0.2059N applied at the tip of section one and zero tip force at the tip of section two. The predicted shape shown in blue color is generated from MATLAB

4.6.4 Comparisons for experiment 1a

The observed and the predicted Cartesian tip coordinates for the both the sections for a range of tip forces are shown in Table 4.1. The percentage error gives the distance

between the Cartesian tip coordinates of both the sections divided by the unstretched reference length of the rod. The average percentage error for section one is less than 1% and for section two it is less than 1.4%, which validates the correctness of the proposed theory.

4.6.5 Experiment 1b: 2D validation of multi-section model

Interesting shapes can be obtained if a force is applied at both sections in the opposite directions. In this experiment, known tip forces are applied in the opposite directions and the corresponding tip coordinates are recorded and compared with the predicted values.

The verification setup has a slight modification in comparison to the previous setup. The setup is shown in Figure 8(b). Due to the design of the verification bench, a known force is applied at section one while the force experienced at the end of section two is measured using a pen scale. Throughout the experiment the length of the cable connected to the pen scale is kept constant. The procedure for performing the experiment is the similar to the previous experiment.

Table 4.1 Observed and predicted results for experiment 1a

	Observed				**Predicted**				**Error**			
	Section 1(cm)		**Section 2(cm)**		**Section 1(cm)**		**Section 2(cm)**		**Section 1**		**Section 2**	
Tip mass (g)	**X**	**Y**	**X**	**Y**	**X**	**Y**	**X**	**Y**	**err(cm)**	**err %**	**err(cm)**	**err %**
2.2	19.5	-1	39	-2.8	19.46	-1.03	38.88	-2.81	0.046	0.238	0.116	0.59
10	19.4	-2.2	38.8	-5.5	19.36	-2.07	38.57	-5.41	0.129	0.661	0.238	1.22
21	19.3	-3.2	38.1	-8.8	19.12	-3.48	37.85	-8.89	0.334	1.716	0.264	1.35
32	18.9	-5	37.2	-12.2	18.77	-4.78	36.85	-12.08	0.248	1.272	0.358	1.84
43	18.5	-6	36	-15	18.36	-5.95	35.67	-14.93	0.138	0.710	0.328	1.68
								Avg err	**0.179**	**0.919**	**0.261**	**1.33**

4.6.6 Comparison for experiment 1b

Table 4.2 shows the Cartesian tip coordinates of both the sections in contrast to the predicted values from the model. Also Figure 11 shows an overlay of the predicted model onto the actual shape of the robot for a tip force of -0.3311 N applied at the tip of section two and 1.01 N applied to the tip of section two. Accuracy of tip predictions of section one are less than 1%; however, for the section two the accuracy is less than 3.4% .The increased error is discussed in the next section.

Table 4.2 Predicted and observed results of experiment 1b

		Observed				Predicted				Error			
Section 1	**Section 2**	**Section 1(cm)**		**Section 2(cm)**		**Section 1(cm)**		**Section 2(cm)**		**Section 1**		**Section 2**	
tipMass (g)	tipMass (g)	X	Y	X	Y	X	Y	X	Y	err(cm)	err %	err(cm)	err %
2.2	0	19.5	-1	39	-3	19.46	-1.02	38.88	-2.78	0.03	0.20	0.23	1.22
9	-3.1	19.5	-1	39	-2.5	19.47	-0.89	38.95	-1.73	0.10	0.55	0.76	3.92
20.5	-6.35	19.5	-1.4	39	-2.5	19.44	-1.34	38.93	-2.08	0.07	0.40	0.42	2.17
32	-9.83	19.5	-1.8	39	-2.5	19.41	-1.70	38.90	-2.16	0.12	0.65	0.34	1.78
43.5	-13.6	19.5	-2	39	-2.5	19.38	-1.97	38.87	-1.94	0.11	0.59	0.56	2.90
55	-17.06	19.5	-2.3	39	-2.5	19.34	-2.32	38.81	-2.01	0.15	0.81	0.51	2.66
66.5	-20.2	19.4	-2.6	38.9	-2.5	19.27	-2.79	38.73	-2.45	0.22	1.17	0.17	0.87
78	-24.53	19.4	-3	38.9	-2.5	19.26	-2.87	38.67	-1.66	0.18	0.96	0.86	4.43
89.5	-27.6	19.4	-3.1	38.8	-2.5	19.17	-3.32	38.57	-2.09	0.31	1.63	0.46	2.40
103	-33.76	19.3	-3.6	38.6	-2.5	19.20	-3.15	38.40	-0.31	0.45	2.34	2.19	11.25
									Avg err	**0.18**	**0.93**	**0.65**	**3.36**

4.6.7 Sources of errors

When performing any experiments it is expected to have errors. The source of errors can be the design of the experiment or how the data is measured. Although from

Table 1 it can be seen that the model is accurate to less than 1.4% in predicting the tip coordinates, from Table 2 the average percentage error has increased to 3.4%.

The average percentage error for section two varies dramatically from 0.875% to 11.25%. However, for section the percentage error variations which vary from 0.2% to 2.34% are not that significant. Hence it can be observed that the model is sensitive to slight changes with respect to the applied external tip force.

The pen scale at section two, acts as a load cell in determining the force at the tip. The sensitivity of the pen scale has a significant impact. The coordinates of the tip of the rod are manually measured and is not accurate to a millimeter scale, the human induced error in obtaining the coordinates could also be a source of error.

4.7 Experiment 2: Effects of cable guides on a single section continuum robot

As discussed previous chapter, two methods were presented in studying the effects of cable guide mass on the backbone. This section verifies the effects of the deformations due to loading produced by cable guide mass. It also experimentally investigates the accuracy of the modeled relationship between shape and cable lengths. A set of five cable guides are placed along the Nitinol rod, separated by 9.5 cm. In addition, a single cable is passed through the five cable guides and terminates at the tip of the rod. A set of loads are then attached to the tip of the rod. For each tip loading, the corresponding Cartesian tip coordinates are measured with the help of the grid. With the help of a small scale, the change in the length of the cable is also measured by using a reference notch. The complete verification setup is shown in Figure 4.10.

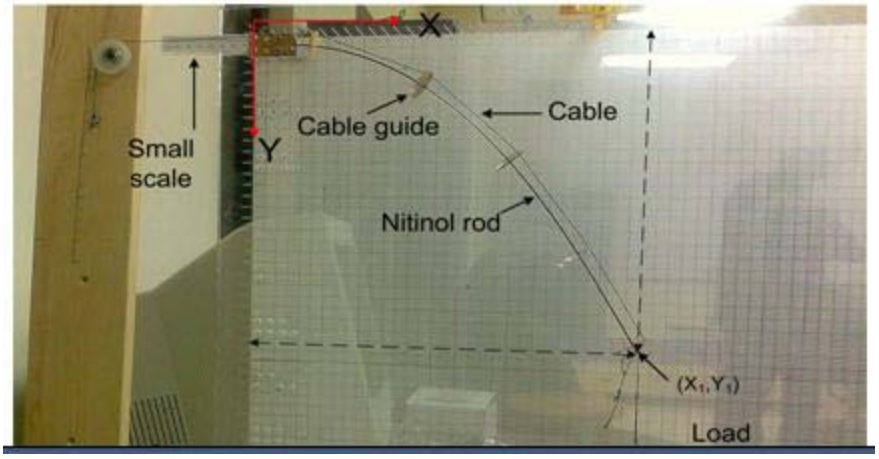

Figure 4.10 Experimental setup for the studying the effects of rod shape and corresponding cable lengths on a Nitinol backbone. Figure 13 shows a detailed photo of the small scale

4.7.1 Cable guide experiment overview

The Nitinol rod with the cable guides is mounted carefully on the vise with the help of levels. A set of five different loads ranging from 0 to 83.2 grams are attached to the tip of the rod. Once the rod settled, the tip coordinates are measured with the help of the grid. For the cable length calculations, a reference notch was tied at the end of the cable as shown in the Figure 13. The location of the notch is recorded at zero tip loading. This value is taken as reference length; as the tip is then loaded with a mass, the change in the position of the notch is recorded

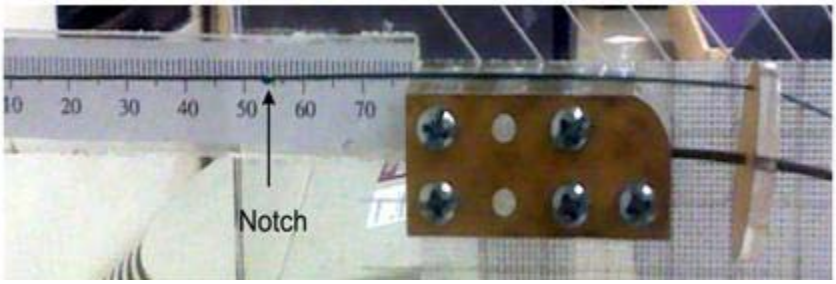

Figure 4.11 Shows a reference notch on the cable. Deflection of the rod changes the position of the notch.

4.7.2 Average mass model

To obtain data from the average model, the first step is to enter the physical properties of the Nitinol rod mechanical details of Nitinol can be found under backbone of continuum robot section discussed in the beginning of the chapter. Next, the combined weight of the rod with cable guides was measured with a pen scale to be 14.9 grams. To obtain modeled locations for cable guide centers, the ODE45 solver is required to compute its results at a set of specific locations corresponding to the five cable guides present on the rod. The final step is recording the observed tip locations for various tip masses. Figure 4.12 shows an overlapped image of the actual versus observed shape of the rod. Note that the even though the predicted shape of obtained from the model is straight line, this is due to the nature of the solver, which only outputs locations at the requested points while internally computing a smooth curve for the reminder of the rod. The locations of the cable guides are hard coded in the model which forces the ODE solver to solve the equations at that particular location. Table 4 summarizes the tip locations of the observed versus the actual shape of the rod.

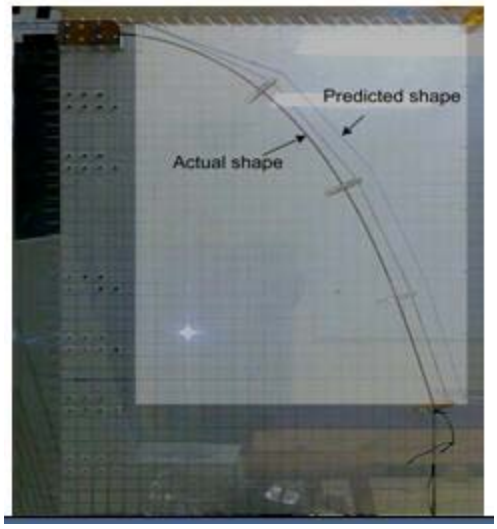

Figure 4.12 Shows comparison of the predicted versus actual shape for a tip mass of 83.2 grams. Note that the predicted shape shown in blue color is in straight lines due to the nature of the solver

Table 4.3 Predicted and observed results of average mass model

	Observed		Predicted		Error	
	Tip of rod		Tip of rod		Tip of rod	
Mass (g)	x_act	y_act	x_pred	y_pred	err(cm)	err %
0	38.8	-6.8	38.42	-6.24	0.674	1.729
17.2	33.3	-18.9	33.09	-18.86	0.205	0.527
27.2	30.5	-22.7	29.91	-22.77	0.591	1.516
40.2	27	-26.1	26.57	-25.89	0.471	1.209
62.2	22.5	-29.3	22.58	-28.77	0.532	1.364
83.2	19.9	-31	19.96	-30.31	0.688	1.764
				Avg err	**0.495**	**1.269**

4.7.3 Accurate mass model

The first step in obtaining the data from the accurate model is by entering the physical properties of the Nitinol rod and the cable guide. The next step is to require the MATLAB ODE45 solver to integrate the differential equations at the locations of the cable guides on the rod. The primary difference between the average and accurate mass models is the way the shear strains $\mathbf{v}^{l}(s)$ are computed. As discussed in the previous

chapter, the following readings are taken from the Nitinol rod which are used in the analytical computation of $\mathbf{v}^l(s)$: the number of cable guides $N = 5$, offset $o = 0.39$ cm, $y = 2.495$ mm and the cable guide spacing $G = 9.5$ cm. The data obtained from the model is fitted with the observed data and the elasticity of the rod was found to be 62.7 GPa. Table 3 shows the observed versus the predicted Cartesian tip locations of the tip of the rod.

The accurate mass model although it physically reflects the structure of the rod with the cable guides does not produce an increase in the overall measured error. From a computation perspective it is reasonable to use the average mass model because the overall percentage error is comparable with the accurate model.

Table 4.4 Predicted and observed results of accurate mass model

	Observed		Predicted		Error	
	Tip of rod		Tip of rod		Tip of rod	
Mass (g)	x_act	y_act	x_pred	y_pred	err(cm)	err %
0	38.8	-6.8	38.42	-6.24	0.674	1.729
17.2	33.3	-18.9	33.09	-18.86	0.205	0.527
27.2	30.5	-22.7	29.91	-22.77	0.591	1.516
40.2	27	-26.1	26.57	-25.89	0.471	1.209
62.2	22.5	-29.3	22.58	-28.77	0.532	1.364
83.2	19.9	-31	19.96	-30.31	0.688	1.764
				Avg err	**0.495**	**1.269**

4.7.4 Deflection of cable length

The method adopted for calculating the change in the length of the cable for a given tip load is same for both accurate and average mass models. The cable deflection analysis begins by measuring the length of the cable at zero tip loading. This is reference length, for subsequent tip loads the measured change in length is subtracted with the

reference length. Table 5 summarizes the deflection analysis for the average and accurate mass models.

In particular, Table 5 is filled out as follows. There are two reference lengths refLenObs and refLenPre. The refLenObs refers to reference length of the cable for an unloaded tip measured on the small scale as per Figure 4.13 and was measured as 4.7 cm, and the refLenPre stands for reference length predicted by the model for a zero tip mass and is found to be 38.72cm.for the average mass model and 38.75cm for the accurate mass model. For each tip loading the change in the length of the cable is recorded and entered in the observed column abbreviated as obs. The delta column gives the change in length with respect to the observed reference length. The changes in the length predicted by the model are calculated in similar way. Finally the percentage error is the difference of the observed and predicted delta. The same procedure is used for both accurate and average mass readings.

Table 4.5 Predicted and observed deflection readings

		Avg mass model				Acc mass model			
obs(cm)	delta(cm)	pred(cm)	delta(cm)	del dif (cm)	Err/reflen	pred(cm)	delta(cm)	delta(cm)	Err/reflen
4.7	0	38.72	0	0	0	38.75	0	0	0
5.2	0.5	39.18	0.458	0.041	0.083	39.19	0.434	0.066	0.132
5.3	0.6	39.32	0.597	0.002	0.004	39.32	0.5697	0.030	0.050
5.5	0.8	39.42	0.705	0.095	0.118	39.43	0.674	0.126	0.157
5.6	0.9	39.52	0.796	0.103	0.115	39.52	0.7632	0.136	0.152
5.7	1	39.55	0.833	0.166	0.166	39.55	0.800	0.199	0.199
			Avg err	**0.0819**	**0.0977**			**0.111**	**0.138**

4.7.5 Sources of errors

Although the percentage error of the tip of the rod for average and accurate mass model is less than 1.5%, the error in measured versus modeled deflection of the cables is significant. Due to elastic nature of the material, the model and the physical rod are very sensitive to external forces. There are mainly two sources of error in the experiment. The cable guides might slip from the rod on repeated usage because they are press fitted to the rod. Since the location of the cable guides are hard coded in the code, there might be some differences in the observed versus the predicted values. Secondly, the observed reading could be off because the rod is attached to the grid using clamps. Due to manufacturing tolerance in the clamps, the rod might not be aligned to exit the clamps at the claimed angle of $0°$.

4.8 Conclusion

This chapter verified two models in 2D presented in the previous chapter. A nickel titanium alloy, Nitinol, was chosen as the backbone for the experiments; for the multi-section validation two experiments were conducted. In the first experiment an external load is applied at the tip of the first section and the second section is left free. For the second experiment both the sections are loaded with a known force. The validation concludes by recording the Cartesian tip locations for a set of known forces.

This chapter also verifies the effects of cable guide mass on a single section rod. Five cable guides laser cut from acrylic sheet were press fit on the Nitinol rod. A thin cable is then passed through these five cables and terminated at the tip of the rod. As set of known weights are attached to the tip of the rod and the Cartesian tip coordinates are recorded. Finally the experiments conclude by comparing the tip locations with the model. The results show that the developed multi-section model is accurate to within

3.4% in predicting the Cartesian tip coordinates and the model with the cable guides shows less than 1.26% error in predicted versus the observed Cartesian tip coordinates of the trunk with the cable guides. However the verification process was limited to 2D and results are for a static model which motivates for a future work discussed in the next chapter.

CHAPTER V

CONCLUSION AND FUTURE WORK

5.1 Conclusion

This thesis presents a 3D model of a multi-section continuum robot and provides experimental verification for the proposed model. The accessibility of a continuum robot, which significantly improves the ability to place the tip of the continuum trunk at a desired location within its workspace, can be enhanced by using a multi-section model. The statics of a single section continuum robot which lay foundations for developing the multi-section model are presented in chapter two.

The next chapter shows the necessary modifications required to expand a single section model to correctly describe multiple sections. The analysis for a multi-section model begins by the definition of a section transition. This transition on the backbone of the continuum robot is treated as a discontinuity and the necessary jump conditions are derived by applying mechanics and kinematics. Next the foundations for a cable driven continuum robot are presented by determining the effects of cable guide mass on the model. The additional mass of the cable guide has been studied using two methods, namely the average mass and accurate mass models. Also, the change in the length of the cable for given tip loading is calculated, which provides an excellent alternative to force and torque measurement in predicting the shape of the robot.

Chapter four presents the verification of the proposed models. A shape memory alloy made of a nickel titanium alloy is chosen as the backbone of the continuum robot. A

set of five circular cable guides, laser cut from acrylic, are press fit on nickel-titanium backbone. The main component of the verification bench is the laser-etched grid which is used in recording the tip coordinates for a loaded backbone. Two sets of experiments were performed on the grid. The first experiment validated the multi-section model by mounting the rod on the grid and applying loads at the end of both the first and second section. The second experiment verifies the effects of cable guide mass by mounting the rod with five cable guides then measuring its tip location. In both the experiments, the Cartesian tip coordinates are recorded and compared with the predicted values which are generated from the model developed in MATLAB.

Finally, the results of this thesis show that the developed multi-section model is accurate to within 3.4% in predicting the Cartesian tip coordinates when both the sections are loaded and to within 1.33% in predicting the Cartesian tip coordinates when only section one is loaded. The model with the cable guides shows less than 1.26% error in predicted versus the observed Cartesian tip coordinates of the trunk with the cable guides for the accurate mass model and 1.44% for the average mass model.

Hence the results show that the multi-section model is accurate and due to the inclusion of cable guides there is significant change in the overall mass of the system. However, the average mass model can be used due to the similarity in results observed among the both the methods.

5.2 Future Work

Future work includes designing a 3D verification test bench. Also, throughout the experiments, only the tip of the continuum robot has been verified; however, methods to compare and contrast all the points on the rod should be formulated. The essential step

for modeling continuum robots is dynamics. The work presented in this thesis lays a foundation for multi-section dynamics and real time shape computation. These shape and the tip predictions can be better visualized by building physical multi-section continuum robot with a nickel-titanium alloy and with a set of stepper motor

REFERENCES

[1] W. M. Kier and K. K. Smith, "Tongues, tentacles and trunks: the biomechanics of movement in muscular-hydrostats," *Zoological Journal of the Linnean Society,* vol. 83, pp. 307-324, 1985.

[2] H. Tsukagoshi, A. Kitagawa, and M. Segawa, "Active Hose: an artificial elephant's nose with maneuverability for rescue operation," in *Proceedings of the IEEE International Conference on Robotics and Automation*, Seoul, Korea, 2001, pp. 2454-2459.

[3] H. Tsukagoshi, A. Kitagawa, T. Koyama, and M. A. Kitagawa, "Mobile method of active hose passing through the narrow space," 2002, pp. 841-846.

[4] S. Ma, S. Hirose, and H. Yoshinada, "Development of a Hyper-redundant Multijoint Manipulator for Maintenance of Nuclear Reactors," *International Journal of Advanced Robotics,* vol. 9, pp. 281-300, June 1995.

[5] F. Thomann, M. Betemps, and T. Redarce, "The development of a bendable colonoscopic tip," in *International Conference on Robotics and Automation*, Taipei, Taiwan, 2003, pp. 658-663.

[6] G. Chen, G. Thomann, M. Betemps, and T. Redarce, "Identification of the flexible actuator of a colonoscope," 2003, pp. 3355-3360 vol.3.

[7] G. Chen, G. Thomann, M. T. Pham, M. Betemps, and T. Redarce, "Modeling and control of a colonoscopic tip under disturbance of the insertion of colonoscope," in *Proceedings of the IEEE/RSJ International Conference on Intelligent Robots and Systems*, Sendai, Japan, 2004, pp. 3315-3320.

[8] G. Chen, P. M. Tu, T. R. Herve, and C. Prelle, "Design and modeling of a micro-robotic manipulator for colonoscopy," in *5th Intl. Workshop on Research and Education in Mechatronics*, Annecy, France, 2005, pp. 109-114.

[9] G. Chen, M. T. Pham, and T. Redarce, "Development and kinematic analysis of a silicone-rubber bending tip for colonoscopy," in *Proceedings of the IEEE/RSJ International Conference on Intelligent Robots and Systems*, Beijing, China, 2006, pp. 168-173.

[10] W. S. Grundfest, I. J. W. Burdick, and A. B. Slatkin, "Robotic endoscopy," U. S. Patent, Ed., 1994.

[11] W. S. Grundfest, I. Burdick, Joel W., and A. B. Slatkin, "Robotic endoscopy," U. S. Patent, Ed. USA, 1997.

[12] K. Ikuta, M. Tsukamoto, and S. Hirose, "Shape memory alloy servo actuator system with electric resistance feedback and application for active endoscope," 1988, pp. 427-430 vol.1.

[13] Y. Bailly and Y. Amirat, "Modeling and Control of a Hybrid Continuum Active Catheter for Aortic Aneurysm Treatment," in *Proceedings of the IEEE International Conference on Robotics and Automation*, Barcelona, Spain, 2005, pp. 936-941.

[14] R. J. Webster, A. M. Okamura, and N. J. Cowan, "Toward Active Cannulas: Miniature Snake-Like Surgical Robots," in *IEEE/RSJ International Conference on Intelligent Robots and Systems*, Beijing, China, 2006, pp. 2857-2863.

[15] R. J. Webster, III, J. S. Kim, N. J. Cowan, G. S. Chirikjian, and A. M. Okamura, "Nonholonomic Modeling of Needle Steering," *The International Journal of Robotics Research,* vol. 25, pp. 509-525, May 1 2006.

[16] M. Ivanescu, M. C. Florescu, N. Popescu, and D. A. P. D. Popescu, "Coil function control problem for a hyperredundant robot," in *IEEE/ASME International Conference on Advanced Intelliget Mechatronics*, Zurich, Switzerland, 2007, pp. 1-6.

[17] R. J. Webster and B. A. Jones, "Design and Kinematic Modeling of Constant Curvature Continuum Robots: A Review," *The International Journal of Robotics Research, forthcoming,* 2010.

[18] B. A. Jones, R. L. Gray, and K. Turlapati, "Three dimensional statics for continuum robots," in *Proceedings of the IEEE/RSJ International Conference on Intelligent Robots and Systems*, St. Louis, MO, USA, 2009, pp. 2659-2664.

[19] S. S. Antman, *Nonlinear Problems of Elasticity* vol. 107. New York: Springer-verlag, 1995.

[20] R. J. Webster, N. J. Cowan, G. S. Chirikjian, and A. M. Okamura, "Nonholonomic Modeling of Needle Steering," in *9th International Symposium on Experimental Robotics*. vol. 21 Singapore: Springer Tracts in Advanced Robotics, 2004, pp. 35-44.

[21] G. Immega, K. Antonelli, and J. Ko, "Teleoperation of the KSI Tentacle Manipulator for hot cell decontamination," in *Proceedings of the IEEE International Conference on Intelligent Systems for the 21st Century*, Vancouver, Canada, 1995, pp. 2133-2136.

[22] B. A. Jones, M. Csencsits, W. McMahan, V. Chitrakaran, M. Grissom, M. Pritts, C. D. Rahn, and I. D. Walker, "Grasping, manipulation, and exploration tasks with the OctArm continuum manipulator," in *video in Proceedings of the International Conference on Robotics and Automation*, Orlando, FL, USA, 2006.

[23] S. S. Antman, *Nonlinear problems of elasticity*, 2nd ed. New York: Springer, 2005.

[24] S. Neppalli and B. A. Jones, "Design, Construction, and Analysis of a Continuum Robot," in *Proceedings of the International Conference on Intelligent Robots and Systems*, San Diego, CA, USA, 2007, pp. 1503-1507.

[25] W. McMahan, B. A. Jones, V. Chitrakaran, M. Csencsits, M. Grissom, M. Pritts, C. D. Rahn, and I. D. Walker, "Field trials and testing of the OctArm continuum manipulator," in *Proceedings of the International Conference on Robotics and Automation*, Orlando, FL, USA, 2006, pp. 2336-2341.

[26] S. Neppalli, B. A. Jones, M. Csencsits, W. McMahan, V. Chitrakaran, M. Grissom, M. Pritts, C. D. Rahn, and I. D. Walker, "OctArm - Soft Robotic Manipulator," in *video in Proceedings of the International Conference on Intelligent Robots and Systems* San Diego, CA, USA, 2007.

[27] W. McMahan, B. A. Jones, and I. D. Walker, "Design and implementation of a multi-section continuum robot: Air-Octor," in *Proceedings of the IEEE/RSJ International Conference on Intelligent Robots and Systems*, Edmonton, Canada, 2005, pp. 3345-3352.

[28] N. Simaan, "Snake-Like Units Using Flexible Backbones and Actuation Redundancy for Enhanced Miniaturization," in *Proceedings of the IEEE International Conference on Robotics and Automation*, Barcelona, Spain, 2005, pp. 3023-3028.

[29] P. Sears and P. Dupont, "A Steerable Needle Technology Using Curved Concentric Tubes," in *Proceedings of the IEEE/RSJ International Conference on Intelligent Robots and Systems*, Beijing, China, 2006, pp. 2850-2856.

[30] D. Trivedi, A. Lotfi, and C. D. Rahn, "Geometrically exact dynamic models for soft robotic manipulators," in *IEEE/RSJ International Conference on Intelligent Robots and Systems*, San Diego, CA, 2007, pp. 1497-1502.

[31] B. A. J. D. Caleb Rucker, and Robert J. Webster, III, "A Geometrically Exact Model for Externally Loaded Concentric-Tube Continuum Robots," in *IEEE TRANSACTIONS ON ROBOTICS,*, OCTOBER 2010, p. 11.

[32] N. Simaan, R. Taylor, and P. Flint, "A dexterous system for laryngeal surgery," in *Proceedings of the IEEE International Conference on Robotics and Automation*, 2004, pp. 351-357 Vol.1.

[33] B. A. Jones and I. D. Walker, "Kinematics for Multisection Continuum Robots," *IEEE Transactions on Robotics,* vol. 22, pp. 43-55, Feb. 2006.

[34] G. Immega and K. Antonelli, "The KSI tentacle manipulator," in *Proceedings of the IEEE International Conference on Robotics and Automation*, Nagoya, Japan, 1995, pp. 3149-3154.

[35] M. W. Hannan and I. D. Walker, "Kinematics and the Implementation of an elephant's trunk manipulator and other continuum style robots," *Journal of Robotic Systems,* vol. 20, pp. 45-63, Feb. 2003.